Delft University of Technology

On the accuracy of data assimilation algorithms for dense flow field reconstructions

Sciacchitano, A.; Leclaire, B.; Schröder, A.

DOI
10.1007/s00348-025-03969-3

Publication date
2025

Document Version
Final published version

Published in
Experiments in Fluids

Citation (APA)
Sciacchitano, A., Leclaire, B., & Schröder, A. (2025). On the accuracy of data assimilation algorithms for dense flow field reconstructions. *Experiments in Fluids*, *66*(2), Article 42. https://doi.org/10.1007/s00348-025-03969-3

Important note
To cite this publication, please use the final published version (if applicable).
Please check the document version above.

Copyright
Other than for strictly personal use, it is not permitted to download, forward or distribute the text or part of it, without the consent of the author(s) and/or copyright holder(s), unless the work is under an open content license such as Creative Commons.

Takedown policy
Please contact us and provide details if you believe this document breaches copyrights.
We will remove access to the work immediately and investigate your claim.

This work is downloaded from Delft University of Technology.
For technical reasons the number of authors shown on this cover page is limited to a maximum of 10.

Experiments in Fluids (2025) 66:42
https://doi.org/10.1007/s00348-025-03969-3

RESEARCH ARTICLE

On the accuracy of data assimilation algorithms for dense flow field reconstructions

A. Sciacchitano[1] · B. Leclaire[2] · A. Schröder[3,4]

Received: 23 August 2024 / Revised: 9 December 2024 / Accepted: 16 January 2025 / Published online: 4 February 2025
© The Author(s) 2025

Abstract

Within the framework of the European Union Horizon 2020 project HOMER (Holistic Optical Metrology for Aero-Elastic Research), data assimilation (DA) algorithms for dense flow field reconstructions developed by different research teams, hereafter referred to as the participants, were comparatively assessed. The assessment is performed using a synthetic database that reproduces the turbulent flow in the wake of a cylinder in ground effect, placed at the distance of one diameter from a lower wall. Downstream of the cylinder, this wall continues either in the form of a flat steady wall, or of a flexible panel undergoing periodic oscillations; these two situations correspond to two different test cases, the latter being introduced to extend the evaluation to fluid–structure interaction problems. The input data for the data assimilation algorithms were datasets containing the particle locations and their trajectories identification numbers, at increasing tracer concentrations from 0.04 to 1.4 particles/mm^3 (equivalent image density values between 0.005 and 0.16 particles per pixel, *ppp*). The outputs of the DA algorithms considered for the assessment were the three components of the velocity, the nine components of the velocity gradient tensor and the static pressure, defined in the flow field on a Cartesian grid, as well as the static pressure on the wall surface, and its position in the deformable wall case. The results were analysed in terms of errors of the output quantities with respect to the ground-truth values and their distributions. Additionally, the performances of the different DA algorithms were compared with that of a standard linear interpolation approach. The velocity errors were found in the range between 3 and 11% of the bulk velocity; furthermore, the use of the DA algorithms enabled an increase of the measurement spatial resolution by a factor between 3 and 4. The errors of the velocity gradients were of the order of 10–15% of the peak vorticity magnitude. Accurate pressure reconstruction was achieved in the flow field, whereas the evaluation of the surface pressure revealed more challenging. As expected, lower errors were obtained for increasing seeding concentration. The difference of accuracy among the results of the different data assimilation algorithms was noticeable especially for the pressure field and the compliance with governing equations of fluid motion, and in particular mass conservation. The analysis of the flexible panel test case showed that the panel position could be reconstructed with micrometric accuracy, rather independently of the data assimilation algorithm and the seeding concentration. The accurate evaluation of the static pressure field and of the surface pressure proved to be a challenge, with typical errors between 3 and 20% of the free-stream dynamic pressure.

1 Introduction

In the recent years, three-dimensional velocity measurements by Particle Image Velocimetry (PIV) have evolved from cross-correlation-based volume analysis (Elsinga et al. 2006; Scarano 2012) to tracking of individual particles (Particle Tracking Velocimetry, PTV, Malik et al. 1993; Lagrangian Particle Tracking, LPT, Schanz et al. 2016, Schröder & Schanz 2023). One of the main advantages of the particle tracking approaches lies in the increased measurement spatial resolution, because a velocity (and acceleration) vector is determined along each and every reconstructed particle trajectory, without averaging such information within a spatial

✉ A. Sciacchitano
a.sciacchitano@tudelft.nl

1 Faculty of Aerospace Engineering, Delft University of Technology, Delft, The Netherlands

2 DAAA, ONERA, Institut Polytechnique de Paris, 92190 Meudon, France

3 DLR, Institute of Aerodynamics and Flow Technology, Göttingen, Germany

4 Chair of Image Based Measurement Techniques, BTU Cottbus-Senftenberg, Cottbus, Germany

sub-domain. However, the particle tracking approaches return velocity vectors at the scattered locations where the tracer particles are present. For data reduction purposes, it is often convenient to map such information onto a regular (Cartesian) grid, to facilitate the operations required for the computation of relevant flow properties such as the vorticity, the Q- or λ_2-criteria for vortex identification and the shear rate, among others. Additionally, the evaluation of the pressure field via the direct integration of the pressure gradient or the solution of the Poisson equation for pressure (van Oudheusden 2013) is typically performed on a regular grid, although grid-less approaches for the solution of the Poisson equation have also been proposed. Conventional techniques to map scattered flow information onto a regular grid involve the use of interpolation (usually linear or cubic interpolation) or spatial averaging of the particle velocities and accelerations over sub-domains or bins (e.g. adaptive Gaussian windowing technique, AGW, Agüí and Jimenez 1987). However, these approaches suffer from low spatial resolution, because they are incapable to resolve flow wavelengths smaller than the inter-particle distance or the bin linear size. As a result, they lead to spatial modulation of the flow field and unresolved or under-resolved length scales, especially for the study of turbulent flows where a wide range of length scales is present. The use of prior information on the flow physics, e.g. by imposing the conservation of mass for incompressible flows via application of a solenoidal filter to the retrieved velocity field (Schiavazzi et al. 2014; Azijli and Dwight 2015), has been shown as a viable methodology to attenuate the measurement noise and enhance the accuracy of the measured flow field. More advanced data assimilation approaches have been recently proposed to enforce the compliance of the resulting flow field with the governing equations of fluid motion, aiming at increasing the range of length scales resolved, possibly beyond the limit of Nyquist criterion. In the FlowFit algorithm introduced by Gesemann et al. (2016) for example, the velocity field is divided into cubic volumes, where it is represented as a weighted sum of 3rd-order 3D base splines. The spline functions are evaluated by solving an optimization problem, where a cost function is minimized that imposes physical constraints such as the conservation of mass and momentum for incompressible flows (Ehlers et al. 2020). In the SPICY algorithm (Sperotto et al. 2024), an analytical representation of the velocity and pressure fields is computed using penalized and constrained Radial Basis Functions (RBFs), which allow enforcing physical constraints as well as boundary conditions. Alternative approaches involve the use of vortex methods (Christiansen 1973), which make use of the vorticity transport equation at one time instant (Schneiders et al., 2016, Cakir et al. 2022) or during a short time sequence (Jeon et al. 2018; Scarano et al. 2022; Jeon 2021) to retrieve a vorticity field compatible with the measured particle velocities and accelerations. Variational methods involving the velocity–pressure formulation of the incompressible Navier–Stokes equations, and stemming from the domain of computational fluid dynamics, have also been proposed to achieve four-dimensional data assimilation accounting for experimental and model errors (Chandramouli et al. 2020) or to reconstruct a full instantaneous flow field, including acceleration data, from a single PTV snapshot (Mons et al. 2022). A recent comparison between 4D-VAR and Physics-Informed Neural Networks (PINNs, Cai et al., 2021) has been conducted by Du et al. (2023), showing that the former exhibit higher accuracy in the assimilation of under-resolved turbulent data, whereas the latter feature higher robustness to measurement noise.

The discussion above highlights the presence of a multitude of approaches aiming at combining flow measurements by LPT and background information on the flow physics to accurately reconstruct the flow field on a regular grid. The aim of this work is to comparatively assess different data assimilation approaches using a database from a simulated experiment, so as to shed light on the capabilities of these approaches and on which parameters and error sources have the largest influence on their performance.

The present work is structured as follows. Section 2 describes the database used for the assessment of the DA algorithms, discussing the physical problem under investigation, the details of how such physical problem was simulated and how the synthetic experiment was set up, and the outputs requested to the participants. In Sect. 3, we describe the different DA algorithms employed by the research groups who analysed the database. The results of the assessment are presented in Sect. 4, first focusing on the rigid wall case (Sect. 4.1) and then on the flexible panel case (Sect. 4.2). For both cases, the results are presented in terms of error statistics of the estimated velocity, velocity gradients and static pressure. Finally, the main conclusions of this work are summarized in Sect. 5.

2 Database description

2.1 Physical problem

A synthetic database was generated that reproduces the experimental parameters encountered in a typical LPT experiment. The turbulent wall-bounded flow in the wake of a cylinder was chosen because of the large turbulent fluctuations, both in velocity and static pressure, associated with the vortex shedding mechanisms. The cylinder diameter $D=0.01$ m, the distance between cylinder and wall $G=0.01$ m, as well as the location of the synthetic flow domain used (extent and streamwise position with respect to the cylinder) were selected to ensure conventional vortex shedding behaviour while maintaining large enough wall pressure fluctuations, both in the flow and on the lower wall; these parameters have been chosen in particular based on the experimental works of Choi & Lee (2000) and Wang & Tan (2008). Numerical simulations were performed using air as working fluid, at a free-stream velocity of 10 m/s, density of $\rho = 1.22$ kg/m^3 and kinematic viscosity of $\nu = 1.503 \cdot 10^{-5}$ m^2/s. The free-stream Reynolds number per unit length was set to $Re_{\infty,x}$ = 665,000, leading to a turbulent boundary layer upstream of the cylinder with a momentum thickness Reynolds number of $Re_\theta \approx$ 4,150, measured 100 mm (ten diameters) upstream of the cylinder centre, and a thickness $\delta \approx$ 60 mm. Two different configurations were considered for the wall downstream of the cylinder. In the first configuration, the wall is a flat rigid wall. An illustration of the flow field for the rigid wall case, along with the reference system of axes, is shown in Fig. 1. The origin of the axes is located at the centre of the wall, and the systems of axes are defined such that X is the streamwise direction, Y the lateral direction and Z the wall-normal direction. In the second configuration the wall is composed of a flexible panel with clamped edges, whose upstream edge is 15 mm downstream of the cylinder. The flexible panel test case was introduced to assess the DA algorithms for unsteady fluid–structure interaction problems, whereby the motion of a solid surface affects the flow field. The panel has dimensions of 100 mm × 100 mm and spans the entire width of the computational domain; it is actuated at its midpoint via a periodic sinusoidal excitation of amplitude A = 5 mm and frequency f_{panel} = 100 Hz. Two materials are considered for the panel, namely metal (more precisely aluminium, Young's modulus E = 70 GPa, density ρ_{metal} = 2700 kg/m^3) and rubber (hyperelastic material with ρ_{rubber} = 950 kg/m^3, C_{10} = 1.3333 MPa and $D_1 = 10^{-9}$ Pa^{-1}), both of thickness t = 0.5 mm. Because the frequency of the vortex shedding from the cylinder is $f_{Shedding} = 200Hz$, the panel motion frequency is in the same order of the vortex shedding frequency; hence, the panel motion is expected to affect the fluctuations in the flow field. The presence of a curved wall introduces new challenges to the DA algorithms in terms of the application of boundary conditions, which are usually enforced only on a Cartesian grid. Additionally, with the flexible panel test case we want to assess how accurately the different DA algorithms are capable of evaluating the position of a relatively complex geometry and in turn the surface distribution of the static pressure. The latter is a crucial parameter in fluid–structure interaction problems, whereby the aerodynamic loads are dominated by the static pressure distribution on solid surfaces and drive the structural motion.

2.2 Details of the flow simulation

Monotone Integrated Large Eddy Simulations (MILES) were performed with the ONERA HPC multi-block structured aerodynamic solver FASTS (see, e.g. Dandois et al. 2018, for an example of application), using second-order finite volume spatial discretization and second-order implicit time integration. The computational domain size is of $1.8m \times 0.1m \times 1.0m$ in the streamwise (X), spanwise (Y) and wall-normal (Z) directions, with mesh cell number of $1367 \times 500 \times 247 = 168{,}824{,}500$ cells. The cell size in the flow region was $\Delta X = 0.4mm$, $\Delta Y = 0.2mm$ and $0.0165mm \leq \Delta Z \leq 0.47mm$. Simulations were run at free-stream Reynolds per unit length and Mach numbers equal to $Re_{x,\infty}$ = 665,000 and M_∞ = 0.07, respectively. The latter value of the Mach number was chosen so as to stay within the accuracy range of the compressible solver, while targeting a nearly incompressible flow. Periodicity was imposed in the spanwise direction, and the method of Lund et al. (1998) was used to obtain a developed turbulent boundary layer. Time- and span-averaged velocity profiles of the flow

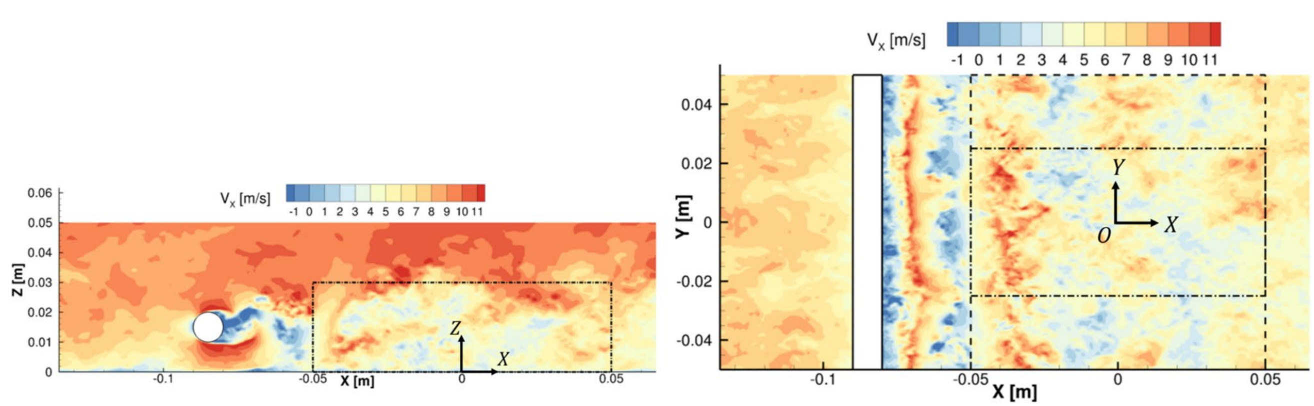

Fig. 1 Side view (left) and top view (right) of the flow domain. The dash-dot rectangle depicts the domain used for the data assimilation analysis for the rigid wall case, whereas the dashed rectangle illustrates the domain for the flexible wall case. Contours of the instantaneous streamwise velocity component are shown; the flow is in the positive X direction. The origin of the system of axes used is indicated with O

observed 100 mm upstream of the cylinder have confirmed the canonical character of the turbulent boundary layer, whose profiles have been found to be in excellent agreement with the literature (LES simulations of Schlatter et al. 2010, corresponding to similar values of the momentum Reynolds thickness Re_θ). Figure 2 shows a sample flow snapshot in the rigid wall case, where the large-scale vortices shed from the cylinder, the secondary vortex structures and their interactions with the wall are visible. Figure 3 presents the corresponding time- and span-averaged mean and fluctuating streamwise velocity components: the flow experiences large velocity fluctuations exceeding 20% of the free-stream velocity, mainly due to the shed vortices and their secondary structures; also, a progressive wake recovery takes place for increasing distances from the cylinder. Although physical conditions differ slightly in terms of the bulk Reynolds

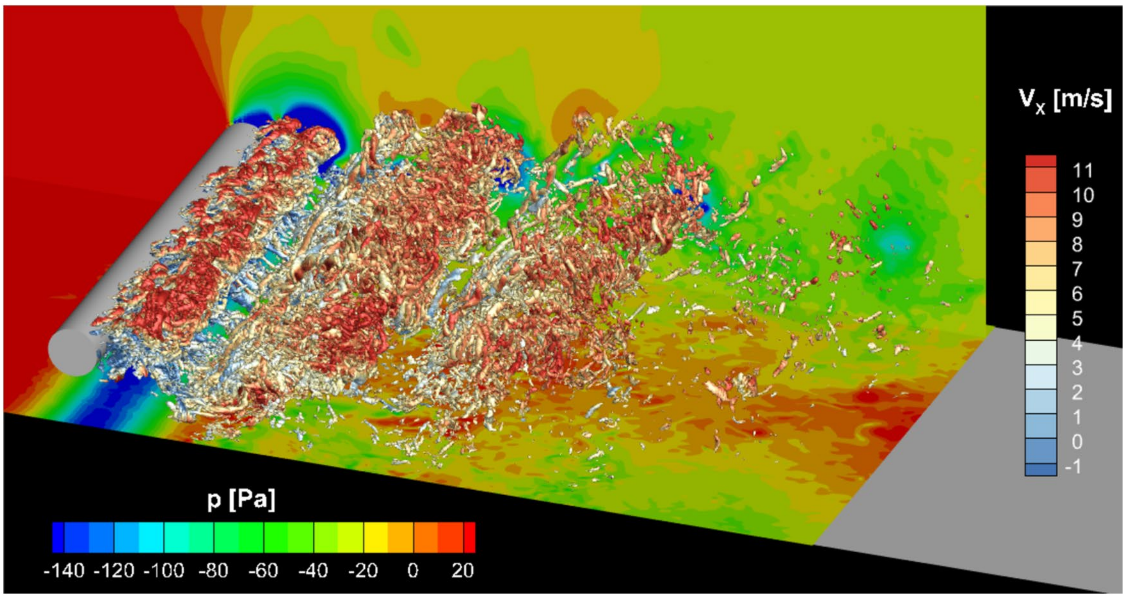

Fig. 2 Sample flow snapshot from the LES simulation (rigid wall case), including Q-criterion iso-surfaces colour-coded by streamwise velocity V_X, and iso-contours of static pressure p at the lower and side walls

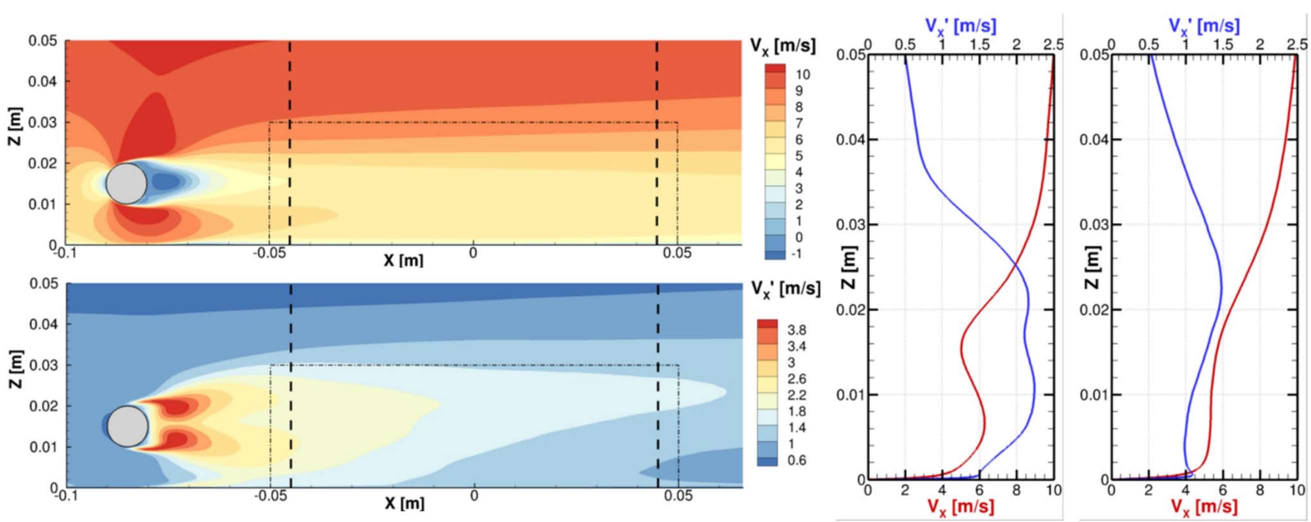

Fig. 3 Left: Streamwise time-average (top) and fluctuations root-mean-square (bottom) velocity components from the LES simulation (rigid wall case), averaged along the span of the simulation domain. The dash-dot rectangle indicates the extent of the flow used for the datasets. Right: profiles of the mean and fluctuating streamwise velocity component, extracted at the locations indicated with vertical dashed lines in the left figures

number, mean velocity profiles such as presented in Fig. 3 agree to a very good extent with the experimental results of Choi & Lee (2000). In the flexible panel cases, the simulation was performed using the Arbitrary Lagrangian Eulerian (ALE) framework (Noh, 1964). Figure 4 illustrates a sample flow snapshot of one of the flexible panel cases (rubber panel), showing the typical values and spatial organization of panel deformation and vertical velocity V_Z, together with cuts of flow streamwise velocity V_X.

Propagation of synthetic pointwise tracer particles, whose positions were initially chosen randomly, was embedded in the simulation using interpolation of the velocity field and a 3rd-order Adams–Bashforth time scheme. Analysis of the trajectories (not shown here) indicated that significant curvatures and accelerations logically coincided mostly with shed vortices, and in a lesser extent with near-wall turbulent structures. While the flow physical configuration was kept for the moving panel cases (air flow with $\rho_{air} = 1.22kg/m^3$, $\nu_{air} = 1.503 \cdot 10^{-5}m^2/s$ at $V_\infty = 10m/s$), for the rigid wall case flow similarity was used to transpose the situation towards a water flow ($\rho_{water} = 998.2kg/m^3$, $\nu_{water} = 9.991 \cdot 10^{-7}m^2/s$) with similar dimensions, thereby leading to free-stream velocity$V_\infty = 0.667m/s$.

2.3 Setup of the synthetic experiments

Synthetic data of the tracer particles were generated based on a hypothetical experimental setup. In particular, virtual multi-camera systems were set up to mimic typical LPT experiments. Following the best practices for three-dimensional flow measurements based on tomographic-PIV and 3D-LPT (Scarano, 2012; Schröder and Schanz 2023), four cameras were simulated for both the rigid and the flexible panel test cases. In the flat rigid wall case, the four cameras were placed along an arc of circle at a radial distance of $R = 0.6m$ from the centre of the data assimilation domain (see Fig. 5). In the flexible panel cases, in order to allow full visualization of the domain (in the spanwise direction), i.e. enclosing all of the panel surface, this distance was increased to $R = 0.9m$.

All virtual cameras had identical properties, namely pixel size of 10 µm, sensor size of 1920 × 1200 pixels and lens focal length f = 100 mm, independently of the panel case. As a result, the difference in their positions leads to slightly different values of the size of a back-projected pixel, hereafter noted as $\overline{px}$, namely $\overline{px} = 60\mu m$ in the rigid wall case, and $\overline{px} = 86.7\mu m$ in the flexible panel cases. This similarly leads to differences in the relationship between the particle image density (counted in particles per pixel, *ppp*) and the volumetric concentration, as seen in Table 1. Overall, image densities ranging from 0.005 to 0.16 *ppp* have been targeted, with three densities for each panel type, with thus

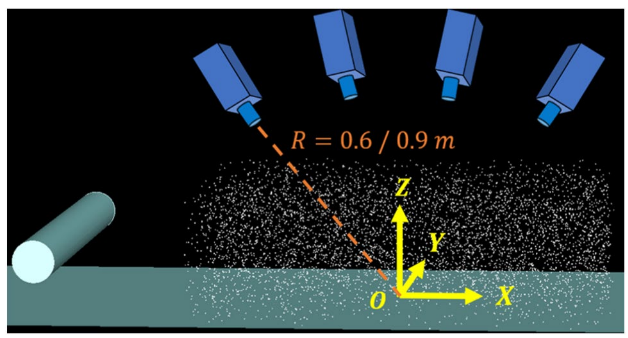

Fig. 5 Sketch of the virtual camera setup

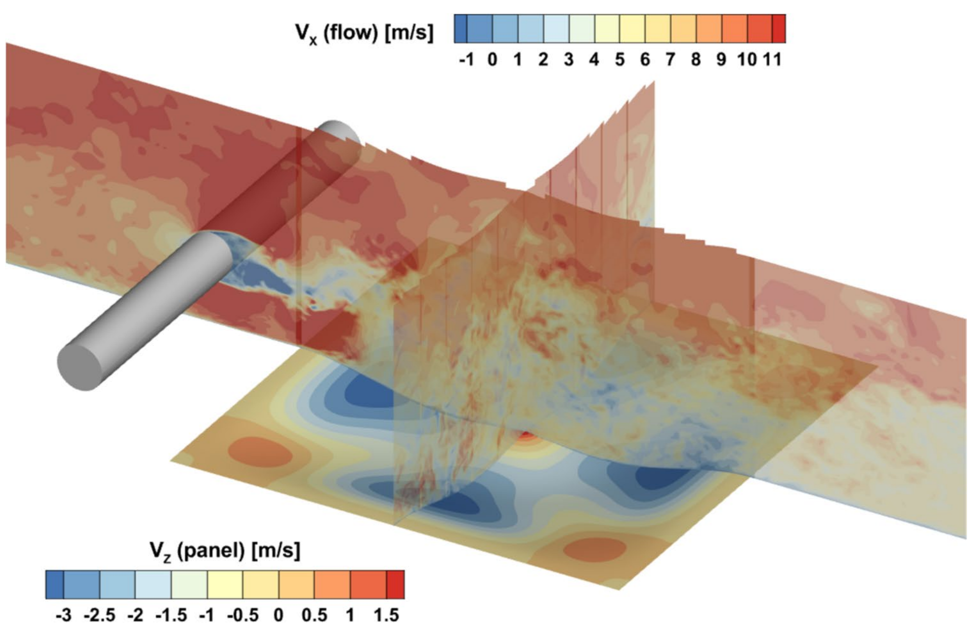

Fig. 4 Sample flow snapshot from the LES simulation (flexible rubber panel case), including iso-contours of flow streamwise velocity V_X in longitudinal and transverse cuts, and of the panel vertical velocity V_Z

Table 1 Main parameters of the datasets composing the DA database. Notice that for the flexible wall case, each dataset is repeated for the two panel materials, namely metal (M) and rubber (R)

Wall	ppp wall markers	ppp flow tracers	# of particles in the fluid domain	Particles concentration C [particles/mm^3]	Average inter-particle spacing λ [mm]
Rigid	0	0.005	6,422	0.0428	1.58
Rigid	0	0.025	31,847	0.212	0.929
Rigid	0	0.160	204,280	1.36	0.500
Flexible, LD (M/R)	0.001	0.022/0.021	23,333/23,268	0.0778/0.0776	1.30
Flexible, LD (M/R)	0.001	0.086/0.081	93,168/92,498	0.310/0.308	0.818/0.820
Flexible, LD (M/R)	0.001	0.171/0.162	185,940/184,058	0.620/0.613	0.650/0.652
Flexible, MD (M/R)	0.01	0.022/0.021	23,295/23,223	0.0777/0.0774	1.30
Flexible, MD (M/R)	0.01	0.085/0.081	92,608/91,941	0.309/0.306	0.820/0.822
Flexible, MD (M/R)	0.01	0.172/0.163	185,903/184,556	0.620/0.615	0.650/0.651

lower maximal particles concentrations (and thus higher inter-particle distances) for the flexible panels than for the rigid cases. These values aim at reflecting experiments ranging from very low to very high seeding densities, compared to the present state-of-the-art of LPT experiments and processing algorithms. In the flexible panel cases, these values correspond to the image densities obtained at the beginning of an oscillating cycle, when the panel is still undeformed. Because the evaluation instant corresponds to a later time, at which the panel exhibits a significant deformation in the vertical downwards (Z) direction, the actual densities in the flexible cases are slightly higher than the targeted values, and slightly different depending on the panel, due to different deformation shapes. Overall, as shown in Table 1, the volumetric particle concentrations range from 0.0428 to 1.36 particles/mm^3, resulting in mean inter-particle distances from 0.5 to 1.58 mm based on Poisson point process theory (Last and Penrose 2017). In the flexible panel cases, markers were placed on the panel at two different densities, namely low density (LD, $ppp = 0.001$) and medium density (MD, $ppp = 0.01$). Due to the different camera arrangement, maximal particles concentrations are lower (inter-particle distances are higher) for the flexible panels than for the rigid cases.

The particle (and marker) positions in 3D space and their trajectories identification numbers were provided to the participants. The particle positions were affected by random Gaussian noise with standard deviation of 0.1 $\overline{px}$, thus corresponding either to $6\mu m$ (rigid wall) or to $8.67\mu m$ (flexible panels); the presence and magnitude of the random noise were not disclosed to the participants. For the rigid wall configuration, the virtual setup was chosen with water as a fluid, with a sequence of 50 equally spaced time instants at time separation $\Delta t = 600$ µs was provided to the participants. For the flexible panel case, coinciding with the original air flow of the simulation, the database contained sequences of 501 evenly spaced time instants at constant time separation $\Delta t = 40$ µs, corresponding to a full period of oscillation. In the metal panel case, both the first and last instants correspond to a flat (undeformed) panel profile coinciding with the $Z = 0$ plane; in the rubber case, the panel is flat at the first instant only, due to the more complex deformation patterns and waves obtained by actuation at the centre point. In both the fixed and moving cases, the time separation leads to a displacement associated with the bulk velocity V_∞ equal to 0.4 mm, i.e. to 6–7 pixels (resp. 4–5 pixels) in the images for the rigid (resp. flexible) cases.

2.4 Requested output

The participants were requested to provide output quantities on a Cartesian grid of spacing $h = 0.4$ mm; details of the Cartesian grids depending on the wall configuration are reported in Table 2.

A total of 13 output quantities were requested, all at the time instant 25 for the rigid wall case and 175 for the flexible panel case; these output quantities were:

- The three components of the velocity vector (V_X, V_Y, V_Z), in m/s;
- The nine components of the velocity gradient tensor $(\partial V_X/\partial X,\ \partial V_X/\partial Y,\ \partial V_X/\partial Z,\ \partial V_Y/\partial X,\ \partial V_Y/\partial Y,\ \partial V_Y/\partial Z, \partial V_Z/\partial X, \partial V_Z/\partial Y, \partial V_Z/\partial Z)$ in s^{-1};
- The static pressure p in Pa, relative to the points $(X, Y, Z) = (0, 0.2, 0.01)$ mm for the rigid wall case, (0, 0, 0.01) mm for the metal panel case and (0, 0, 0.41) mm for the rubber panel case.

Additionally, for the flexible panel case, the Z-position of the panel markers and the static surface pressure were requested. The data were analysed in terms of errors of the output quantities (viz. difference from the actual value from

Table 2 Number of grid points along the different directions and limits of the data assimilation domains for the three wall configurations

	Number of grid points				Limits of the data assimilation domains					
	X	Y	Z	Total	X_{min} (mm)	X_{max} (mm)	Y_{min} (mm)	Y_{max} (mm)	Z_{min} (mm)	Z_{max} (mm)
Rigid wall	251	126	76	2,403,576	–50	+50	–25	+25	+0.01	+30.01
Metal panel	251	251	76	4,788,576	–50	+50	–50	+50	+0.01	+30.01
Rubber panel	251	251	75	4,725,075	–50	+50	–50	+50	+0.41	+30.01

the LES simulation at each grid location), their distributions and spectral content.

3 Participants and approaches

3.1 Rigid wall case

The data of the rigid wall test case were presented and analysed within the first Data Assimilation challenge (Sciacchitano et al. 2021), conducted within the framework of the European Union Horizon 2020 project HOMER (Holistic Optical Metrology for Aero-Elastic Research), grant agreement number 769237.

Three research groups analysed the data of the rigid wall case, namely the German Aerospace Centre from Göttingen (DLR), Delft University of Technology in the Netherlands (TU Delft, shortly TUD) and the German instrumentation company LaVision GmbH. The approaches employed by these groups are briefly summarized hereafter. As reported in Table 3, differences among the algorithms are already present in the way the particle locations are fitted to retrieve the positions, velocities and accelerations at time instant $t=25$, which constitute the inputs for the considered DA approaches.

3.1.1 DLR: FlowFit2

The approach employed by the DLR group is based on the TrackFit and FlowFit2 algorithms, which are described in detail in Gesemann et al. (2016) and in Ehlers et al. (2020). The main processing steps are the following:

(a) Determination of the particle trajectories according to the provided locations and track-ID data;
(b) Spectral analysis of the location-over-time signals to estimate the optimal TrackFit parameters;
(c) TrackFit: estimation of the particle trajectories as uniform cubic B-spline curves;
(d) Sampling of the particle track B-spline functions at the specified time step (namely 25), including first and second derivatives (velocity and acceleration), as input to FlowFit;
(e) FlowFit2: nonlinear estimation of velocity and pressure fields as 3D uniform cubic B-splines based on a weighted least-square optimization that minimizes the sum of several squared errors. Those include: the divergence of the velocity field, the gradient of the divergence of the velocity field, deviations between measured and fitted velocities and accelerations, deviations from the pressure Poisson equation, velocity vector Laplacian.

Before the FlowFit2 step, additional virtual particles with zero velocity and acceleration are generated at the wall ($Z=0$ m) to comply with the no-slip boundary condition.

3.1.2 *TUD: VIC+and TSA*

The TU Delft team made use of two approaches, both based on the Vortex-in-Cell framework (Christiansen 1973). The first approach, named VIC+(Schneiders and Scarano 2016), seeks a vorticity field defined at the output Cartesian grid such that a cost function is minimized. The latter depends on the difference between the measured and reconstructed velocities and Lagrangian accelerations at the particle locations. The velocity field is then obtained from

Table 3 Types and temporal kernel sizes of the fit used to determine the particle positions, velocities and accelerations

Participant (approach)	Track fit type	Track fit temporal kernel size
DLR	Cubic B-spline	Adaptive, based on the spectral analysis of the particle tracks
LaVision (VIC#-3D)	2nd-order polynomial	7/7/9 at $ppp=0.005/0.025/0.160$
LaVision (VIC#-4D)	2nd-order polynomial	7/7/9 at $ppp=0.005/0.025/0.160$
TUD (VIC+)	2nd-order polynomial, 3 iterations	9
TUD (TSA)	2nd-order polynomial, 3 iterations	9

the reconstructed vorticity field via the solution of the Poisson equation. The second approach, named Time-Segment Assimilation (TSA, Scarano et al. 2022), is an evolution of the VIC + concept which exploits the temporal information from time-resolved measurements. In this case, the vorticity dynamics equation is used to march forward and backward for a finite number of exposures (in total 31 at $ppp = 0.005$ and 21 at $ppp = 0.025$) the first guess of the vorticity field at time $t = 0$. The cost function is built as the difference between the measured and the reconstructed velocity at the particle locations along the entire time segment. It should be noted that, due to the high computational cost, the TSA results were only produced for $ppp = 0.005$ and 0.025, and not for $ppp = 0.160$. Additionally, the pressure field was evaluated only for the VIC + analysis (and not for the TSA analysis), by solving the Poisson equation for pressure (van Oudheusden 2013), using Neumann boundary conditions at all boundary points.

3.1.3 LaVision: 3D and 4D VIC#

LaVision GmbH made use of two approaches, one relying only on instantaneous data (3D) and one exploiting the information on the time evolution from time-resolved measurements (4D). In the latter case, the time integration length was selected as $\pm 6\Delta t$, resulting in the simultaneous velocity reconstruction over 13 time steps. The approaches, indicated with VIC#-3D and VIC#-4D, respectively, are based on an evolution of the VIC + algorithm (Schneiders and Scarano 2016) where additional physical constraints on the divergence of velocity, vorticity, Eulerian acceleration, Lagrangian acceleration and on the momentum equation are imposed (Jeon et al. 2018, 2022; Jeon 2021). A multi-grid approximation was performed to decrease the computational cost due to large number of elements in the output Cartesian grid.

3.2 Flexible panel case

The flexible panel data were analysed by the German Aerospace Centre from Göttingen (DLR) and the German instrumentation company LaVision GmbH.

3.2.1 DLR: FlowFit2

As for the rigid wall case, the DLR group made use of the FlowFit2 algorithm (Gesemann et al. 2016; Ehlers et al. 2020), which involved the following steps:

- Spectral analysis of particle and marker trajectories to determine good temporal fitting parameters.
- The particle and marker trajectories were filtered using TrackFit with a cut-off of 0.25 and 0.03 times the Nyquist frequency, respectively. TrackFit behaves like a low-pass filter with a flat passband and an 18 dB/oct slope after the cut-off frequency. For the marker tracks, the filter was slightly modified so that the pass-band response at $f_{panel} = 100$ Hz was exactly 1.0, so as not to suppress any fluctuations at the frequency of oscillation of the panel.
- The cubic B-splines for the particle and marker trajectories were evaluated at the requested time step, namely time step 175.
- For the velocities and accelerations of the panel markers, a 2D curve over x, y was fitted using uniform cubic B-splines and smoothing by penalizing the Laplacian. These fitted 2D functions were evaluated twice, once on the requested x, y grid for the panel and once for the internal reconstruction grid of the FlowFit as "wall conditions".
- FlowFit2 then used the particle data and spatially interpolated marker data (wall conditions) as input. The internal reconstruction grid was chosen to have about 25 grid points per particle.

3.2.2 LaVision: 3D and 4D VIC#-FSI

LaVision made use of an adaptation of VIC# (Jeon et al. 2018, 2022; Jeon 2021) that accounts for the presence of solid objects in the flow domain, named VIC#-FSI. VIC#-FSI considers a moving boundary through artificial surface vectors interpolated from the surface markers. Its computation domain is a rectangular parallelepiped, identical to VIC#. However, the additional constraints of VIC#, including pressure field, are only considered for the fluid region. The surface pressure is afterwards obtained from a least-square optimization of pressure changes between the surface grid points and the surface-facing flow grid points.

As for the rigid wall case, also for the flexible panel case two algorithms where employed: a 3D algorithm, which only accounts for the instantaneous information on the flow and the structural markers, and a 4D algorithm that exploits time information over 13 time steps at $ppp = 0.020$ and 0.080, and 7 time steps at $ppp = 0.160$. Future and past time steps are included in the analysis using a Eulerian time-marching scheme with the 4th-order Runge–Kutta temporal discretization.

3.3 Computational cost

A dedicated analysis has been conducted to assess the computational cost of the different DA approaches. Notice that, despite the participants processed the data on different machines, the computational cost analysis has been performed using the same computer architecture, which featured high-end consumer GPUs (RTX 4090), after the participants had submitted their results. The analysis has been performed on the data of the rigid wall test case, obtaining the following computational times per computed flow field (see Table 4):

The results of Table 4 show clearly that the computational cost varies by up to three orders of magnitude depending on the DA approach. Several factors influence the computational cost. First, the computational domain size affects the number of operations for both the numerical integration and the minimization of the cost function: although the original domain size is composed of 251 × 126 × 76 = 2,403,576 grid points, different algorithms use different extensions of the domain to avoid erroneous velocity reconstructions close to the edges. In particular, the FlowFit 2 algorithm only requires two additional grid points at each edge, thus limiting the size of the computational domain. Conversely, in the case of VIC + and VIC-TSA, the computational domain size is more than three times larger than the original domain size, while for VIC# the increase of domain size is about 15% (6 padding grid points at each edge, Jeon et al. 2022). Second, each method solves a different number of Poisson equations: for FlowFit 2, only one Poisson equation per iteration is solved for the evaluation of the pressure field from the measured velocity data (Ehlers et al. 2020); instead, VIC + requires solving 12 Poisson equations per iteration, namely two per each component of the velocity and of the local Eulerian acceleration. In the case of VIC-TSA, to reduce the computational burden which is already very large, only the velocity components are employed in the definition of the cost function, and not the acceleration; for this reason, only 6 Poisson equations (namely two per velocity component) need to be solved per iteration. Both the three-dimensional and four-dimensional versions of VIC# require solving 13 Poisson equations (Jeon et al. 2022), namely the 12 equations needed for VIC +, plus an additional equation for the static pressure.

Additionally, the computational cost of each method scales proportionally to the number of the limited-memory BFGS iterations (Liu and Nocedal 1989) required for the minimization of the cost function, where the limit is set to 125 for FlowFit 2 and 400 for the other algorithms. It is also worth mentioning that, with respect to their three-dimensional counterparts (VIC#-3D and VIC +), the computational cost of four-dimensional methods (VIC#-4D and VIC-TSA, respectively) increases proportionally to the number of time steps considered. For the reasons above, the FlowFit 2 algorithm is orders of magnitude faster (only a few seconds per flow field) than the other approaches, whereas the methods that employ information from multiple time steps (namely VIC#-4D and VIC-TSA) are the slowest, with a computational cost of O(1000) seconds per reconstructed flow field.

4 Results

4.1 Rigid wall case

4.1.1 Velocity components

The results of the data assimilation algorithms are expected to exhibit an increasing error for decreasing seeding concentration, as a consequence of the larger inter-particle distance and therefore lower spatial resolution. For the intermediate seeding concentration case ($ppp = 0.025$), Fig. 6 compares the streamwise velocity component along several planes in the measurement domain, as well as an iso-surface of the Q-criterion (Q = 80,000 s^{-2}) among ground-truth (top-left), participants' results, and linear interpolation of the particle velocities (bottom right). Note that in the sequel, we will preferentially single out this concentration value ($ppp = 0.025$) for presenting spatial fields of reconstructed quantities and errors, as, out of the values tested, it is the one most typical of common LPT experiments. We recall that the free-stream velocity is equal to $V_\infty = 0.667 m/s$ in the present rigid wall case, as the medium for this case has been chosen to be water (see Sect. 2.2). From the ground-truth

Table 4 Computational cost of the different DA approaches, per flow field

Method	# Time steps	Original domain size (grid points)			Computational domain size (grid points)			# Poisson equations	# L-BFGS iterations	Computational time (seconds)
		X	Y	Z	X	Y	Z			
FlowFit 2	1	251	126	76	255	130	80	1	125	4
VIC +	1	251	126	76	401	202	98	12	400	474
VIC-TSA	21	251	126	76	401	202	98	6	400	4979
VIC-TSA	31	251	126	76	401	202	98	6	400	7349
3D VIC#	1	251	126	76	257	132	82	13	400	180
4D VIC#	3	251	126	76	257	132	82	13	400	540
4D VIC#	5	251	126	76	257	132	82	13	400	900
4D VIC#	13	251	126	76	257	132	82	13	400	2340

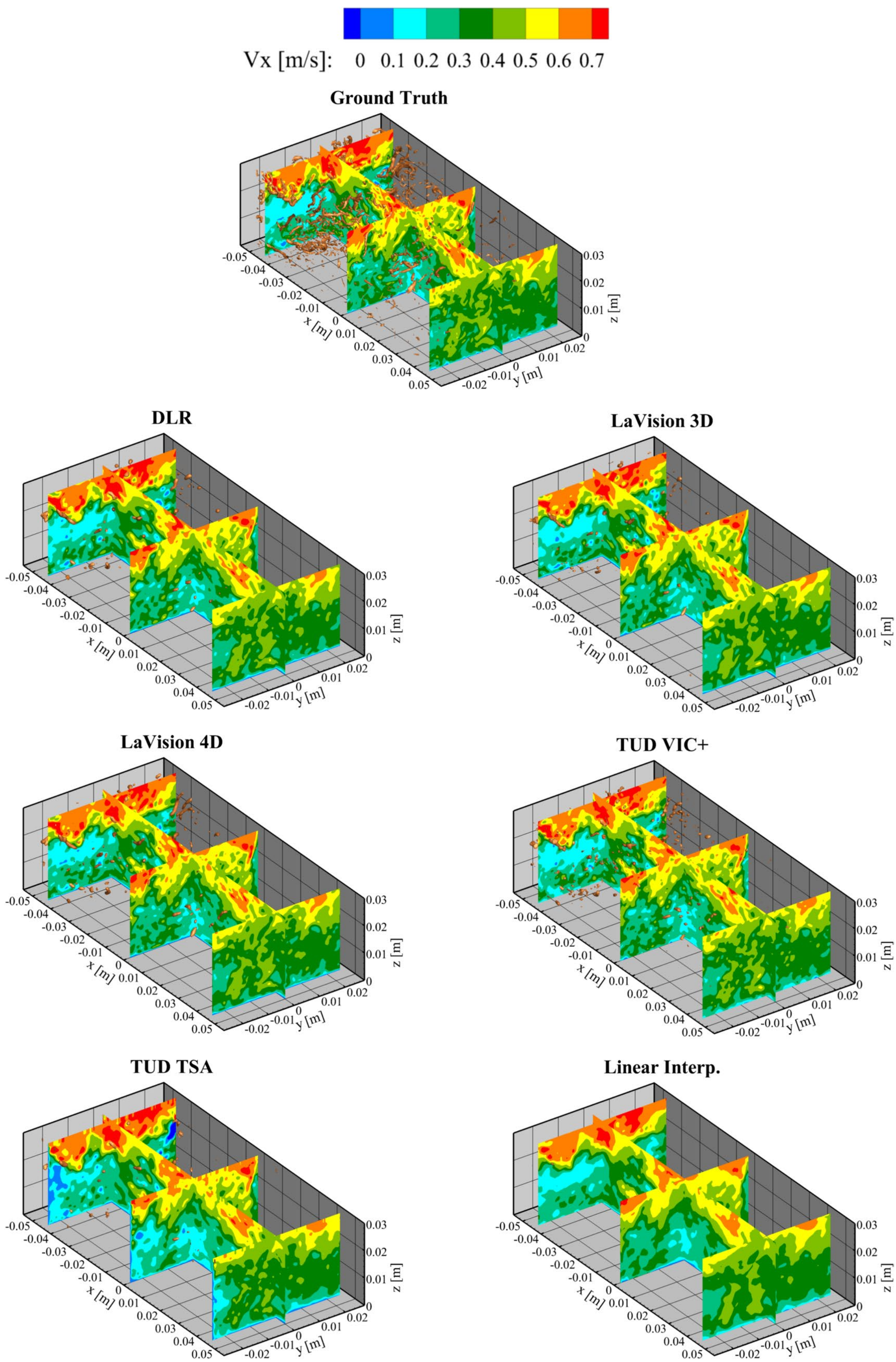
Vx [m/s]: 0 0.1 0.2 0.3 0.4 0.5 0.6 0.7
Ground Truth
DLR
LaVision 3D
LaVision 4D
TUD VIC+
TUD TSA
Linear Interp.
x [m]
y [m]
z [m]

◀**Fig. 6** Slices of the streamwise velocity component and of iso-surfaces of Q-criterion ($Q = 80{,}000\ s^{-2}$) for the *ppp* = 0.025 case. The ground-truth flow field from the numerical simulations is shown on the top. The result from the linear interpolation of the particles velocities onto the Cartesian grid is shown on the bottom right

flow field, the decrease of the velocity towards the wall (Z = 0) due to the presence of the boundary layer is evident. The flow field is clearly turbulent, featuring many small coherent vortical structures visualized via the Q-criterion. The results of the different algorithms are overall similar to the ground truth, in that they correctly reproduce the turbulent nature of the boundary layer and velocity values diminishing towards the wall. The result from TUD TSA exhibits more edge effects especially towards the lower limit of Y, where the streamwise velocity component decreases to unphysical values close to zero. The linear interpolation result correctly reproduces the main characteristics of the flow field, although with a larger spatial modulation, thus resulting in coarser and smoother velocity contours. However, when the small vortical structures are compared in terms of iso-surfaces of Q-criterion, it is clear that none of the data assimilation algorithms (nor the linear interpolation) is able to correctly capture those due to the limited spatial resolution of the measurement.

A more detailed analysis of the estimated velocity and the error relative to the ground truth is reported in Fig. 7 for the plane Y = –0.2 mm, close to the centreline. It is evident that all data assimilation algorithms are capable of reproducing the largest scales of the ground-truth velocity field. Even when linear interpolation of the particle velocities is performed (bottom row), the resulting velocity field shows clear similarity with the ground-truth one, although spatial modulation occurs, which has the effect of smoothening out the small-scale structures. For instance, the positive and negative velocity peaks at X = –0.01 m are significantly attenuated. The absolute errors on the streamwise velocity component, illustrated on the right column of Fig. 7, are mostly below 0.1 m/s (15% of the bulk velocity V_∞), with only a few peaks exceeding 0.15 m/s; their values and distributions are rather independent of the algorithm employed. All of the data assimilation algorithms use physical constraints derived from the equations of motion to reconstruct the flow from the data; the present observations thus indicate that the input data are still not enough resolved for these constraints to reconstruct accurately the finest scales.

A quantitative analysis of the bias and random errors of the velocity magnitude as a function of the seeding concentration is conducted in the entire measurement domain excluding 4 mm (ten grid points) from all the outer edges to avoid edge effects. Such analysis is presented in Fig. 8. The local error is defined as the difference between the velocity estimated by the DA algorithms and the ground-truth value at each grid point; the bias error is the spatial average of the local error, whereas the random error is the spatial standard deviation of the local error. The bias error (Fig. 8-left) exhibits little dependence on the *ppp*, and it typically attains values within 0.5% of the fluid bulk velocity V_∞; such errors increase slightly at the lowest *ppp*, reaching values of 2% of V_∞. The highest errors are encountered with the TUD TSA algorithm, attaining values of up to 4% of V_∞. Also, it is remarked that the linear interpolation algorithm yields similar but slightly larger bias errors to most data assimilation algorithms. The random error, illustrated in Fig. 8-left, shows the expected decrease with increasing seeding concentration. At the lowest *ppp*, the random error is between 0.06 and 0.075 m/s (or 9% and 11% of V_∞) and decreases to about 0.02 m/s (roughly 3% of V_∞) at *ppp* = 0.16. At each seeding concentration, small but systematic differences of about 0.01–0.02 m/s among the different algorithms are recorded. It is noticed that the linear interpolation approach yields random error values of the same order as those of the data assimilation algorithms with the lowest performance. As the following analysis will show, this is due to the fact that the remaining scales, below those reconstructed by linear interpolation, represent only a limited fraction of the flow kinetic energy.

To indeed further assess the capabilities of the data assimilation approaches to resolve small scales in the flow field, a spectral analysis is conducted in a region of the flow domain away from the wall, namely for 20 mm ≤ Z ≤ 30 mm. The spectral analysis is performed by taking the velocity distribution along a line at a fixed Y and Z location and then computing the spatial spectrum of that velocity distribution using Welch's power spectral density method (Welch 1967). The results from all the spectra obtained in the domain $20mm \le Z \le 30mm$ and $-21mm \le Y \le 21mm$ are then spatially averaged. The average power spectral density in such region of the wall-normal velocity component V_Z is illustrated in Fig. 9 for the three *ppp* values. As expected, the different algorithms agree well with the ground-truth results (thick grey lines) at the lower wavenumbers k (larger wavelengths λ), whereas the agreement worsens for increasing wavenumbers. Also expected is the improved agreement with increasing seeding concentration. At the lowest *ppp* of 0.005 (Fig. 9-left), the linear interpolation result departs from the ground truth already at a wavenumber of 50 m^{-1} (or wavelength of 20 mm, that is more than 12 times larger than the average inter-particle distance). In contrast, the data assimilation algorithms follow the ground-truth result up to $k \approx 200\ m^{-1}$ ($\lambda \approx 5mm$), thus yielding an increase of the range of resolved length scales by a factor 4 with respect to the linear interpolation. Similar trends are retrieved also at the higher seeding concentrations (Fig. 9-middle and -right), with improved agreement with the ground-truth result. In particular, at the highest *ppp* of 0.16, most data assimilation

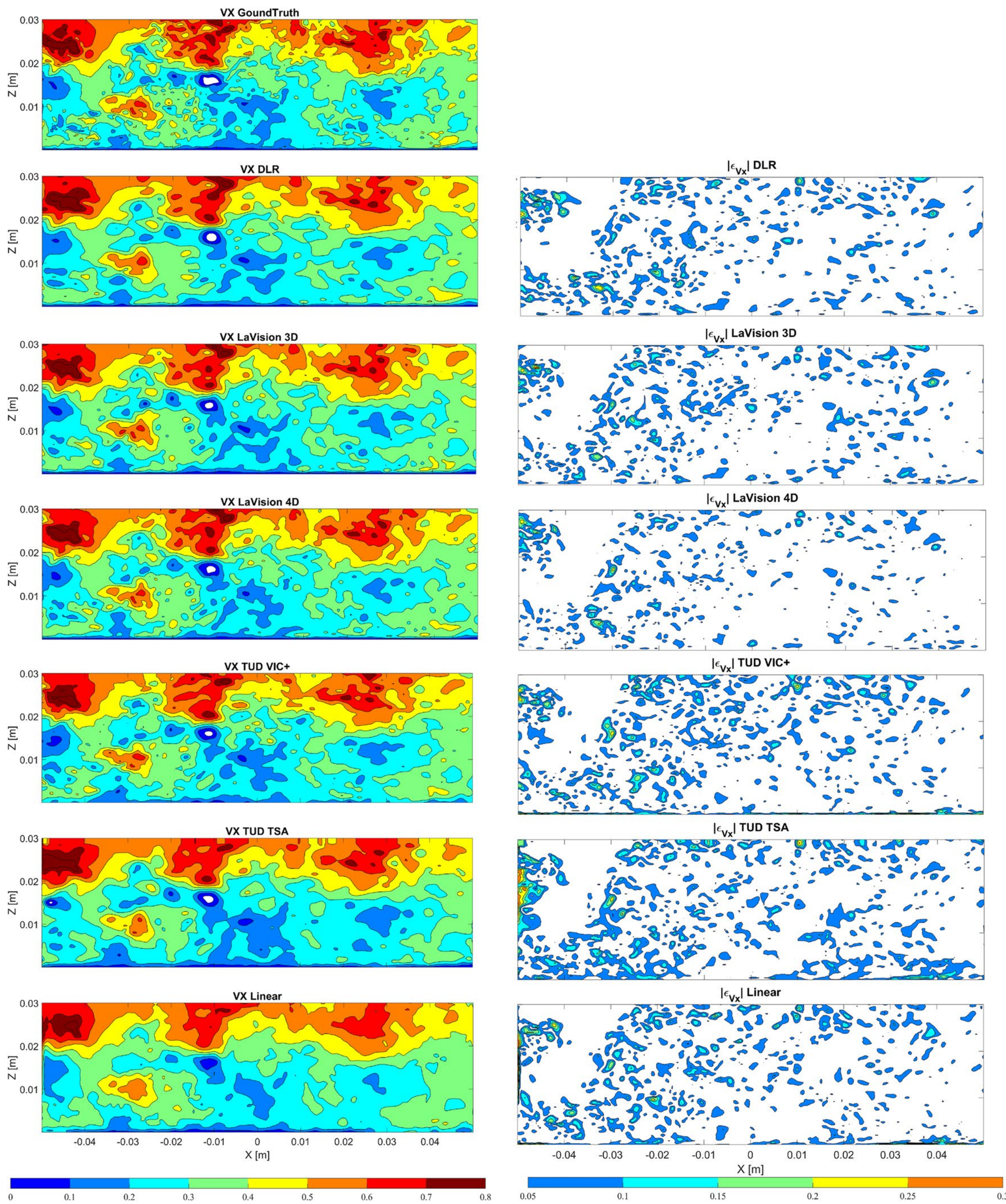

Fig. 7 Streamwise velocity component at mid-span, i.e. here $Y = -0.2$ mm (left) and corresponding absolute error (right) for the $ppp = 0.025$ case. The colorbars at the bottom represent m/s and apply to all contours of the same column

algorithms capture correctly the power spectrum up to $k \approx 300\ \mathrm{m}^{-1}$ ($\lambda \approx 3$mm), whereas the linear interpolation result starts departing from the ground truth already around $k \approx 100\ \mathrm{m}^{-1}$ ($\lambda \approx 10$mm). Hence, based on this spectral analysis, it can be concluded that the data assimilation algorithms increase the range of resolvable length scales by a factor 3 to 4 with respect to the standard interpolation, and that the smallest fluctuations correctly captured occur at a length scale that is 3 to 6 times larger than the average inter-particle distance.

4.1.2 Velocity gradient components

The evaluation of the components of the velocity gradient is notoriously more challenging than that of the velocity itself for two main reasons: first, under-resolved or unresolved

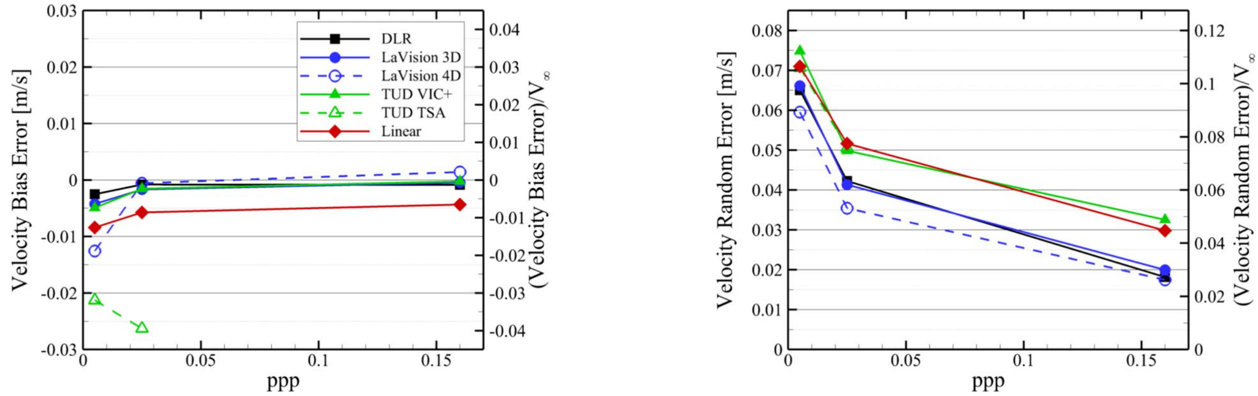

Fig. 8 Bias (left) and random (left) error of the velocity magnitude as a function of the *ppp*. The symbol keys apply to both plots

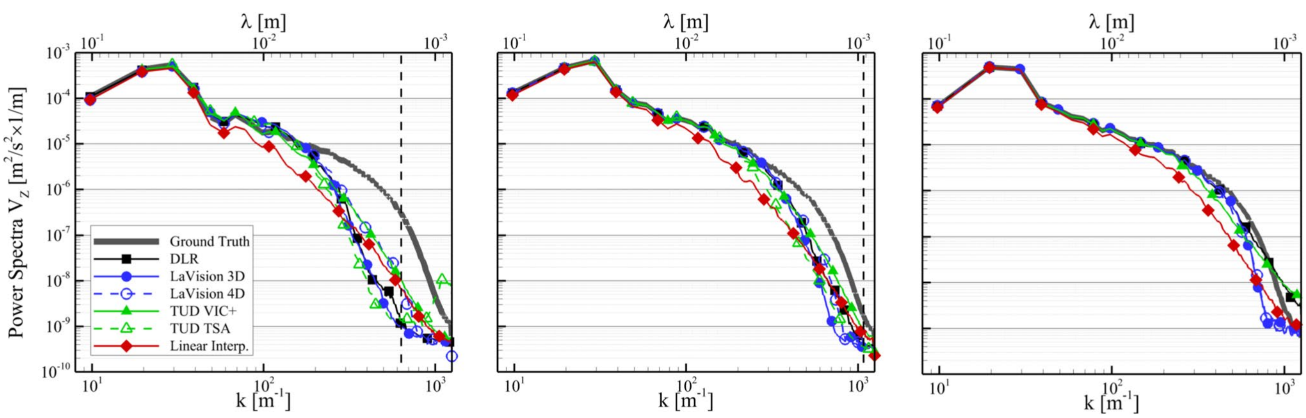

Fig. 9 Power spectral density of the wall-normal velocity component V_Z, averaged in the region 20 mm ≤ Z ≤ 30 mm. Left: *ppp* = 0.005; middle: *ppp* = 0.025; right: *ppp* = 0.16. The bottom horizontal axis represents the wavenumber, while the top horizontal axis represents the corresponding wavelength. The dashed vertical line, when present, corresponds to the wavenumber (or wavelength) associated with the average inter-particle spacing. The symbol keys apply to all plots

length scales result in the underestimation of the spatial derivatives of the velocity; second, the spatial derivative operator acts as a high-pass filter onto the velocity field, thus yielding a decrease of the measurement signal-to-noise ratio in presence of uncorrelated noise. The accuracy of the evaluation of the velocity gradient components is assessed in Fig. 10 via the analysis of the vorticity magnitude and the related error for the case *ppp* = 0.025. The ground-truth vorticity field presents vorticity peaks up to 1000 Hz attributed to small-scale vortical structures especially in the region closer to the cylinder (X < 0). Additionally, a large-scale vortical structure, ascribed to the vortex shedding from the cylinder, with peak vorticity approaching 800 Hz is found around X = –0.1 m. All considered algorithms exhibit a significant modulation of the vorticity field, yielding vorticity peak values seldom exceeding 500 Hz. From the vorticity errors contours presented in the right column of Fig. 10, it can be seen that the vorticity errors exceed 100 Hz in a large portion of the measurement domain, with peaks even above 700 Hz. The largest errors, mainly ascribed to spatial modulation, occur when using the linear interpolation approach.

The vorticity magnitude along a vertical profile extracted at X = –11.2 mm and Y = –0.2 mm is shown in Fig. 11. This profile has been selected because of the presence of a vortex at about Z = 18 mm from the wall, resulting in a peak vorticity of about 750 Hz. All the data assimilation algorithms correctly reproduce the presence of the vortex and the corresponding peak of vorticity. However, the actual value of the peak vorticity is strongly modulated, with a reduction between 21% (LaVision 4D algorithm) and 40% (TUD TSA algorithm). Instead, the different data assimilation algorithms fail to reproduce correctly a second vorticity peak (500 Hz) at 14 mm ≤ Z ≤ 16 mm, yielding a measured vorticity peak between 200 (TUD TSA algorithm) and 300 Hz (LaVision 4D algorithm). This result is ascribed to the smaller size of the vortical structure. It is interesting to notice that all the algorithms predict a lower location of the vorticity peak (Z = 14.4 mm, rather than Z = 15.6 mm),

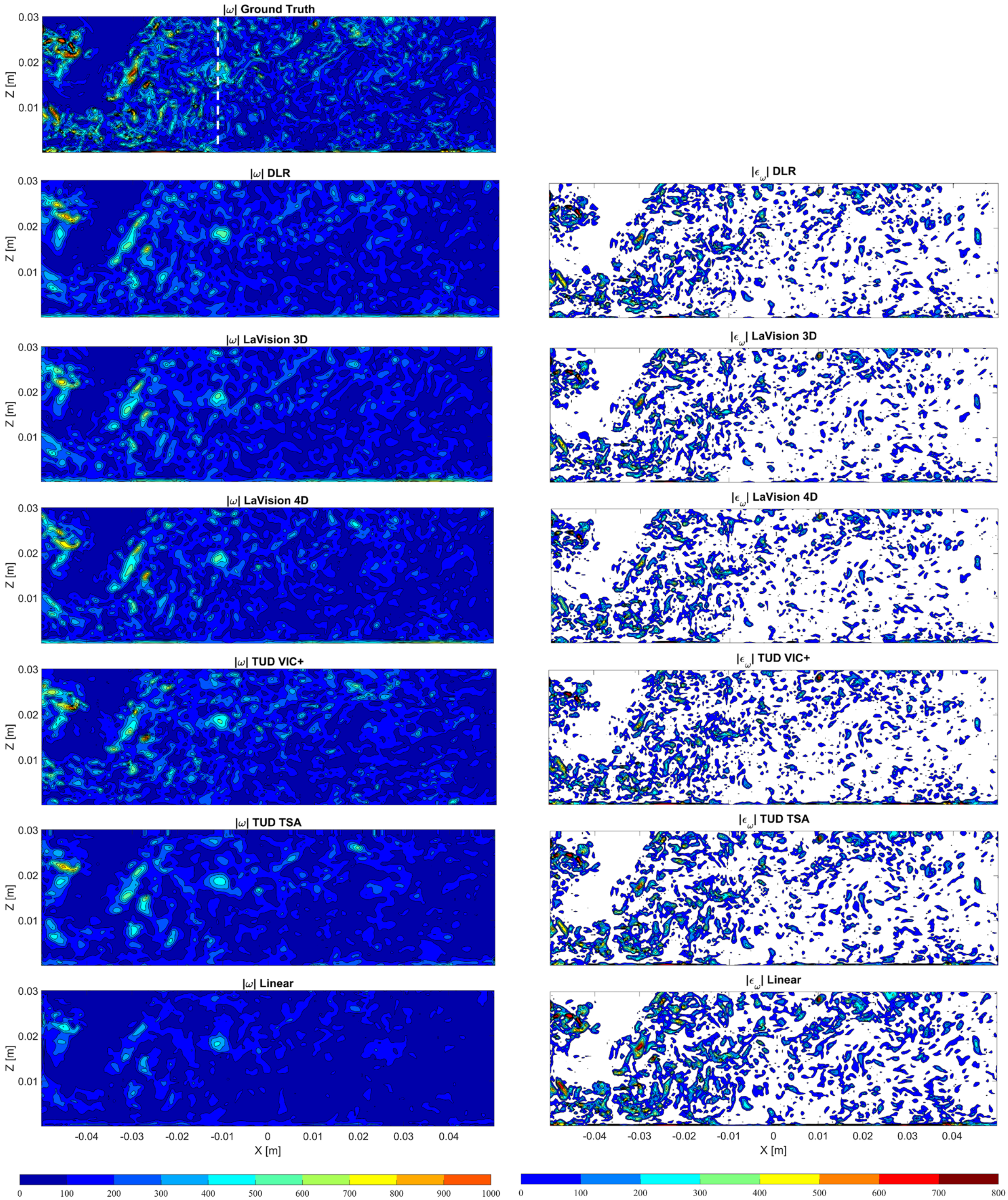

Fig. 10 Vorticity magnitude in Hz at Y=–0.2 mm (left) and corresponding absolute error (right) for the ppp=0.025 case. The white dashed vertical line in the top-left contour corresponds to the location of the profile shown in the next figure. The colorbars at the bottom represent Hz and apply to all the contours of the same column

which is probably caused by the presence of a tracer particle closer to that location.

Similar to the velocity, a quantitative analysis of the vorticity magnitude error is conducted in terms of mean bias and random components in the entire measurement domain, excluding a region of 4 mm thickness at the outer edges. The results of this analysis are shown in Fig. 12. As expected, there is a clear trend of increasing performance

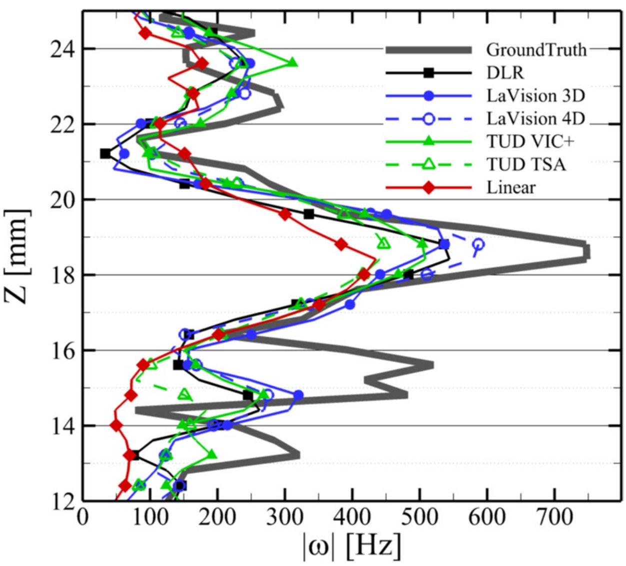

Fig. 11 Vertical profiles of vorticity magnitude at X = –11.2 mm and Y = –0.2 mm, for the *ppp* = 0.025 case

when increasing the seeding concentration. As discussed above, the mean bias errors (Fig. 12-left) are negative as a consequence of the spatial modulation of the velocity field that yields underestimated vorticity values. The DLR algorithm exhibits the best performance in terms of mean bias errors, with error values between −80 Hz at the lowest *ppp* and −20 Hz at the highest *ppp*. Similar values are retrieved also with the LaVision algorithms and the TU Delft VIC + approach. In contrast, the linear interpolation approach returns bias error values between −130 and −80 Hz. The random error component, illustrated in Fig. 12-right, exhibits values of around 150 Hz at *ppp* = 0.005, with small differences among the different algorithms. At higher seeding concentrations, a significant error reduction is retrieved down to 80 Hz and 90 Hz with the DLR and LaVision algorithms, respectively; in contrast, for the other algorithms the random errors remain above 130 Hz (TU Delft VIC +, TSA and linear interpolation approaches). Considering that the ground-truth peak vorticity attains values of about 1000 Hz, it can be concluded that, using the best data assimilation algorithms at the highest *ppp* level of 0.160, the vorticity error values are of the order of 2% and 8% for the bias and random components, respectively. However, these errors increase to 4% and 13%, respectively, when less performing data assimilation algorithms are employed. At the lowest seeding density of *ppp* = 0.005, the bias and random errors can be as large as 8% and 17%, respectively, of the peak vorticity values.

For sake of completeness, the contours of the divergence of the velocity at Y = –0.2 mm are shown in Fig. 13 for the case *ppp* = 0.025. It should be noticed that, because of the low but finite Mach number of the flow cases considered ($M_\infty = 0.07$, this value being nonzero due to the use of a compressible flow solver), based on the conservation of mass for incompressible flows, the divergence of the velocity is expected to be finite as well, but of very small magnitude. In fact, the ground-truth result (Fig. 13 top) exhibits divergence values typically below 0.2 Hz. The results of the different data assimilation algorithms exhibit large differences. The DLR algorithm does not impose zero divergence in the measured flow field; as a result, the measured divergence is nonzero, but mostly bounded to below 1 Hz. Instead, the LaVision algorithms, both 3D and 4D, evaluate a solenoidal (hence divergence-free) flow field, with nonzero divergence values only close to the boundaries. A similar result is obtained with the TU Delft VIC + and TSA algorithms, although a more complex pattern is obtained, with zero divergence only sufficiently away from the boundaries. Instead, the result from linear interpolation yields velocity divergence values well above 1 Hz (median value of $|\nabla \bullet \boldsymbol{V}|$ equal to 21 Hz), indicating that the velocity field does not satisfy the conservation of mass.

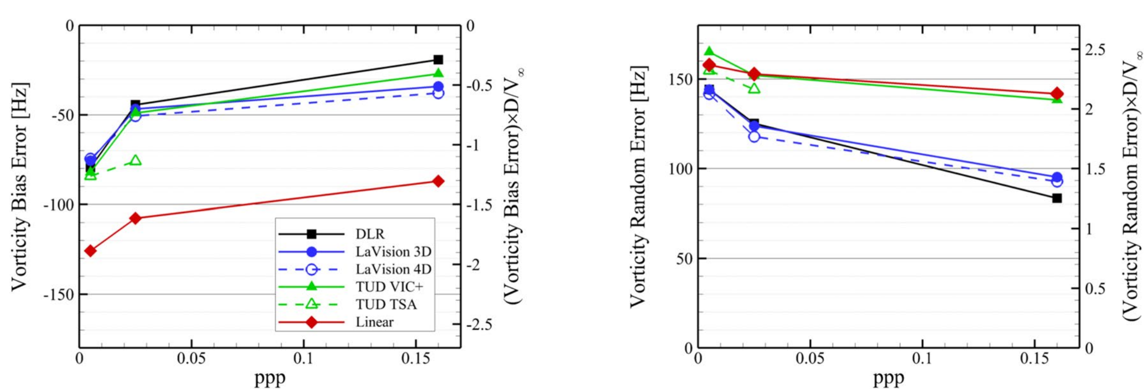

Fig. 12 Bias (left) and random (left) error of the vorticity magnitude as a function of the ppp. The symbol keys apply to both plots

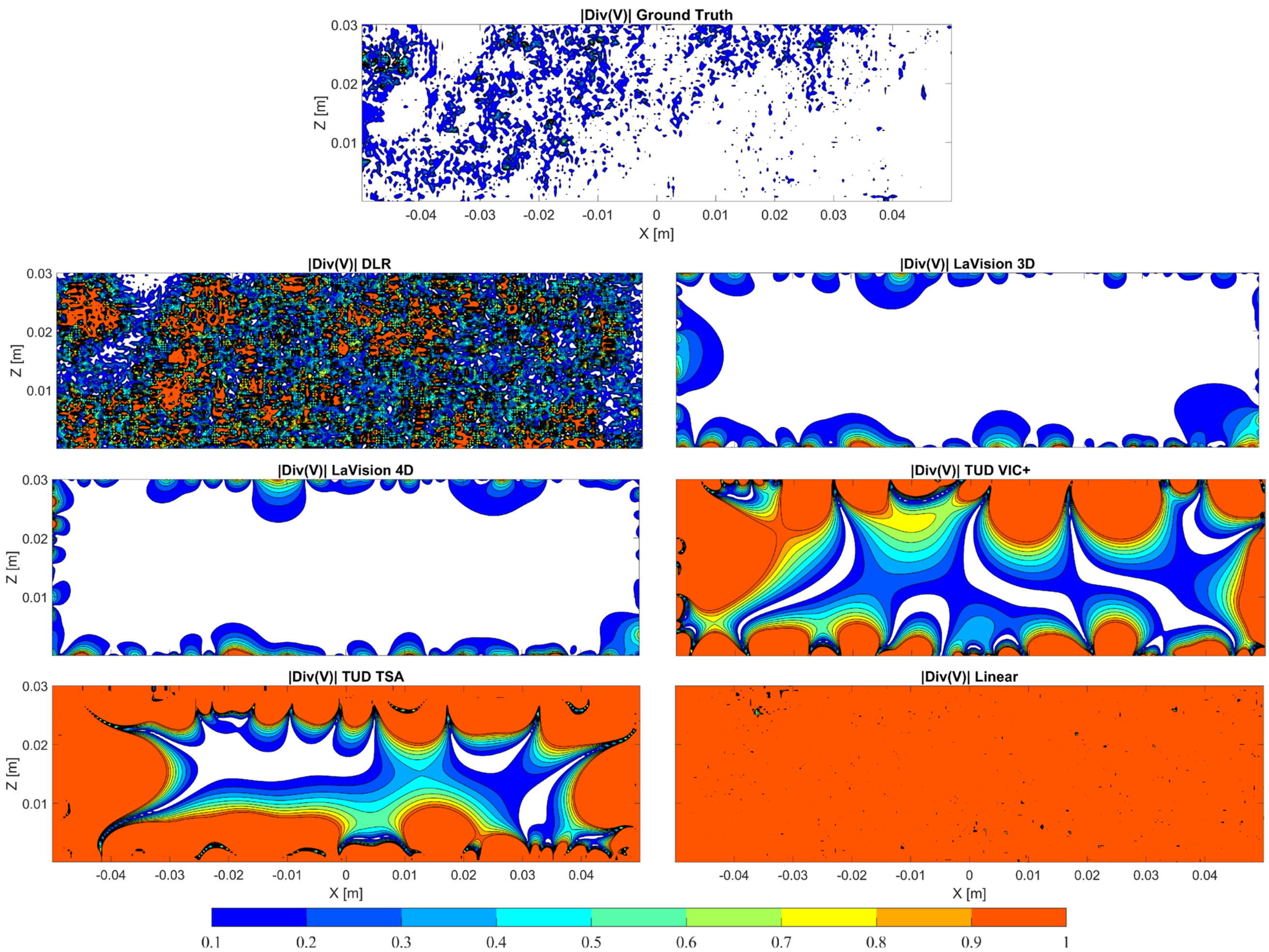

Fig. 13 Absolute value of the divergence of the velocity in Hz at $Y=-0.2$ mm for the $ppp=0.025$ case. The colorbar at the bottom applies to all contours

4.1.3 Static pressure

4.1.3.1 Static pressure in the flow field The pressure gradient is related to the Lagrangian acceleration via the Navier–Stokes equations; evaluation of the pressure field is typically conducted either via direct integration of the pressure gradient or by solving the Poisson equation for pressure (van Oudheusden 2013). Hence, errors in the Lagrangian acceleration propagate to the pressure, although the integration operator is expected to attenuate the contribution of the random errors. Figure 14 illustrates the static pressure field in a plane close to the centreline (Y = –0.2 mm) for the intermediate seeding density case ($ppp=0.025$), along with the corresponding error fields (right column). The ground-truth field shows the presence of three large low-pressure regions at X = –0.04 m, –0.01 m and + 0.026 m, respectively, associated with vortices shed by the cylinder. The minimum pressure values within these regions are about –180 Pa, –220 Pa and –60 Pa, respectively, corresponding to 80%, 100% and 30% of the free-stream dynamic pressure (q_∞ = 221.8 Pa). Additionally, smaller flow features with low pressure are present near X = –0.03 m. All algorithms are capable to reproduce the large low-pressure structures, although not always with the correct pressure magnitude. Most algorithms return correct values of the pressure peak typically within 10%; however, the linear interpolation result[1] overestimates the pressure peak at the upstream edge of the domain by 30% and underestimates the pressure peak at X = + 0.026 m by 50%. The error fields, presented in the second column of Fig. 14, show that the errors are mainly random, although some peaks as high as 50 Pa (or over 20% of the free-stream dynamic pressure) occur at the locations of the low-pressure

[1] The linear interpolation result is obtained by first computing the velocity and Lagrangian acceleration fields based on linear interpolation of the particle information, then computing the pressure gradient as $\nabla p = -\rho DV/Dt$, and finally solving the Poisson equation for pressure with Neumann boundary conditions.

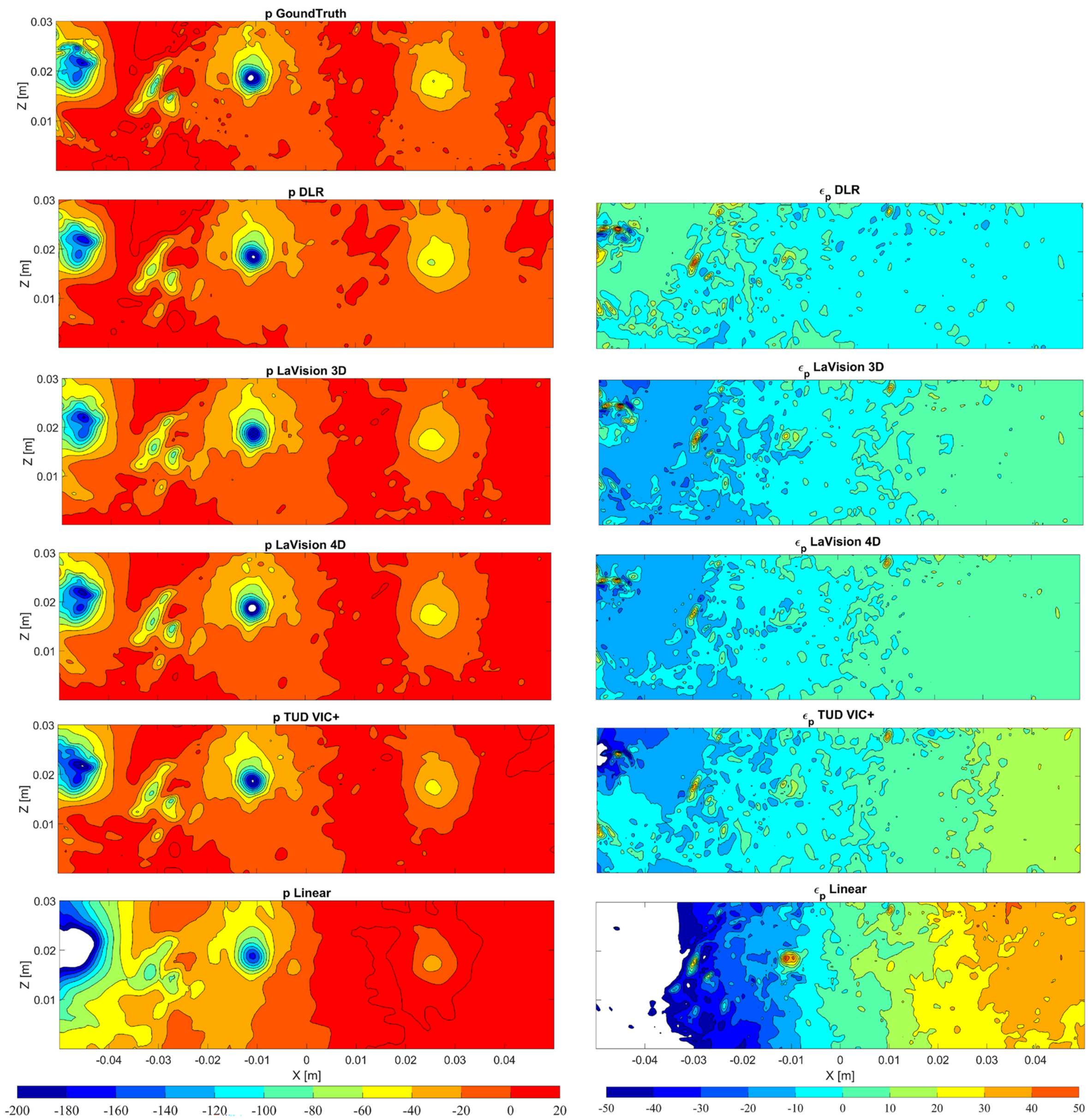

Fig. 14 Static pressure field (left column) and error of the static pressure (right column) at the plane Y = –0.2 mm, for the case *ppp* = 0.025. First row: ground-truth result. The values in the colorbars are in Pascal. The colorbars at the bottom apply to all the contours of the same column. The free-stream dynamic pressure is equal to $\boldsymbol{q}_\infty$ = 221.8 Pa

structures at X = –0.03 m and X = –0.01 m. In the result of the linear interpolation algorithm, the pressure error shows a clear gradient in the horizontal direction, which is attributed to an erroneous estimation of the data at the location where boundary conditions are imposed.

The quantitative analysis of the errors, illustrated in Fig. 15, confirms that the random errors dominate over the bias errors. The latter are typically in the range [–5, 5] Pa, except for the linear interpolation approach. As expected, the accuracy of the pressure reconstruction increases with the seeding density, thus yielding a reduction of the random error component (Fig. 15-middle). However, the random errors curves decrease rapidly up to *ppp* = 0.025, whereas they flatten for higher seeding concentrations. At *ppp* = 0.16, the random errors from the different algorithms range between 4 Pa (less than 2% of q_∞, achieved with the DLR algorithm) and 18 Pa (8% of q_∞, obtained with the linear interpolation approach). Also, it is noticed that the use of temporal information in the data assimilation algorithm slightly improves the pressure reconstruction (see comparison between LaVision 3D and LaVision 4D results, where the latter always yields lower random errors).

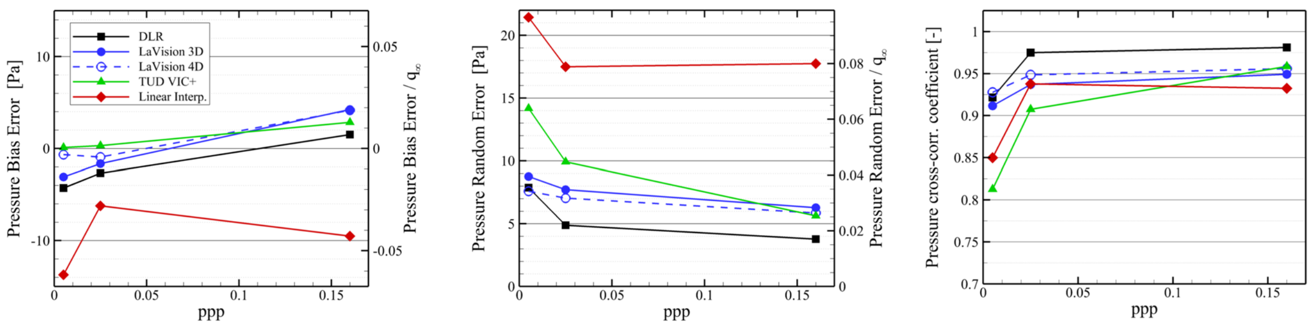

Fig. 15 Mean bias error (left), random error (middle) and cross-correlation coefficient with respect to the ground truth (right) of the static pressure, evaluated at plane Y = –0.2 mm, as a function of the ppp. The errors and cross-correlation coefficient are evaluated over the entire measurement domain, excluding a border of 4 mm (10 grid points) at the outer edges. The symbol keys apply to all plots

The cross-correlation coefficients between the participants' results and the ground-truth pressure field (Fig. 15-right) confirm the capability of the data assimilation algorithm to accurately reconstruct the larger-scale features in the pressure field. For the two higher seeding concentrations, the cross-correlation coefficient is close to or above 0.8, with values even exceeding 0.95 especially at *ppp* = 0.160. As anticipated, the pressure reconstruction is more challenging at the lowest seeding concentration due to the low measurement spatial resolution; in these conditions, the cross-correlation coefficients range between 0.81 (TU Delft VIC + algorithm) and 0.93 (LaVision 4D algorithm).

4.1.3.2 Surface static pressure The evaluation of the static pressure on the surface of solid objects is of great relevance in aerodynamics and fluid–structure interaction problems because it enables to characterize the spatial distribution of the aerodynamic loads. Unfortunately, computing the surface pressure often involves even more challenges than evaluating the static pressure in the flow field, because of the small magnitude of the wall pressure fluctuations, the large velocity gradients in the boundary layer and the presence of unwanted light reflections. The ground-truth pressure field in close proximity of the rigid wall (Z = 0.01 mm), illustrated in Fig. 16-top for the intermediate seeding concentration case (*ppp* = 0.025), confirms that indeed the pressure variations on the surface are a small fraction of those in the flow field; a high-pressure region (pressure values exceeding 10 Pa) is visible in the upstream half of the domain, with an inclination of about 45° with respect to the free-stream direction. Additionally, small-scale flow structures are visible, with pressure values varying between –30 and 30 Pa. The results of the different participants, shown in the first column of Fig. 16, confirm the complexity of the surface pressure reconstruction problem. The result from DLR shows a clear similarity to the ground-truth surface pressure field, especially for what concerns the high-pressure region in the upstream half of the domain. However, spatial modulation effects are present which attenuate the pressure peaks; also, most of the small-scale pressure fluctuations are not resolved. The pressure results from LaVision (both 3D and 4D) and TU Delft VIC + exhibit some similarity to ground-truth result, although they fail to reproduce correctly the high-pressure region. The magnitudes of the errors on the estimated pressure, illustrated in the second column of Fig. 16, are of the same order as the actual pressure fluctuations. Finally, the surface pressure fields from linear interpolation exhibit the largest differences from the ground-truth results. In this case, the errors on the estimated pressure even exceed the actual pressure fluctuations, indicating that the approach is unsuited for the evaluation of the surface pressure.

The quantitative analysis of the mean bias error, random error and cross-correlation coefficient with the ground-truth surface pressure field is presented in Fig. 17. The surface pressure errors are in a similar range as the errors in the rest of the flow field shown in Fig. 15 (bias errors: between –10 and 10 Pa; random errors: between 5 and 20 Pa). However, because of the smaller magnitude of the surface pressure fluctuations, the cross-correlation coefficient drops significantly to values below 0.8. The largest cross-correlation coefficient (0.8) is obtained with the DLR algorithm and is rather independent of the seeding density; in contrast, the other approaches return cross-correlation coefficient values below 0.6, which further drop to even negative values (TUD VIC + algorithm) at the lowest seeding concentration, confirming the poor surface pressure reconstruction accuracy in this condition.

Finally, the results of the spectral analysis on the surface pressure are illustrated in Fig. 18 for the three *ppp* levels. A clear trend is visible of increasing agreement between ground-truth and participants' results at increasing seeding concentration. However, some algorithms (DLR, LaVision 3D and LaVision 4D) underestimate the pressure fluctuations at all wave numbers, whereas the linear interpolation approach tends to overestimate them, thus resulting

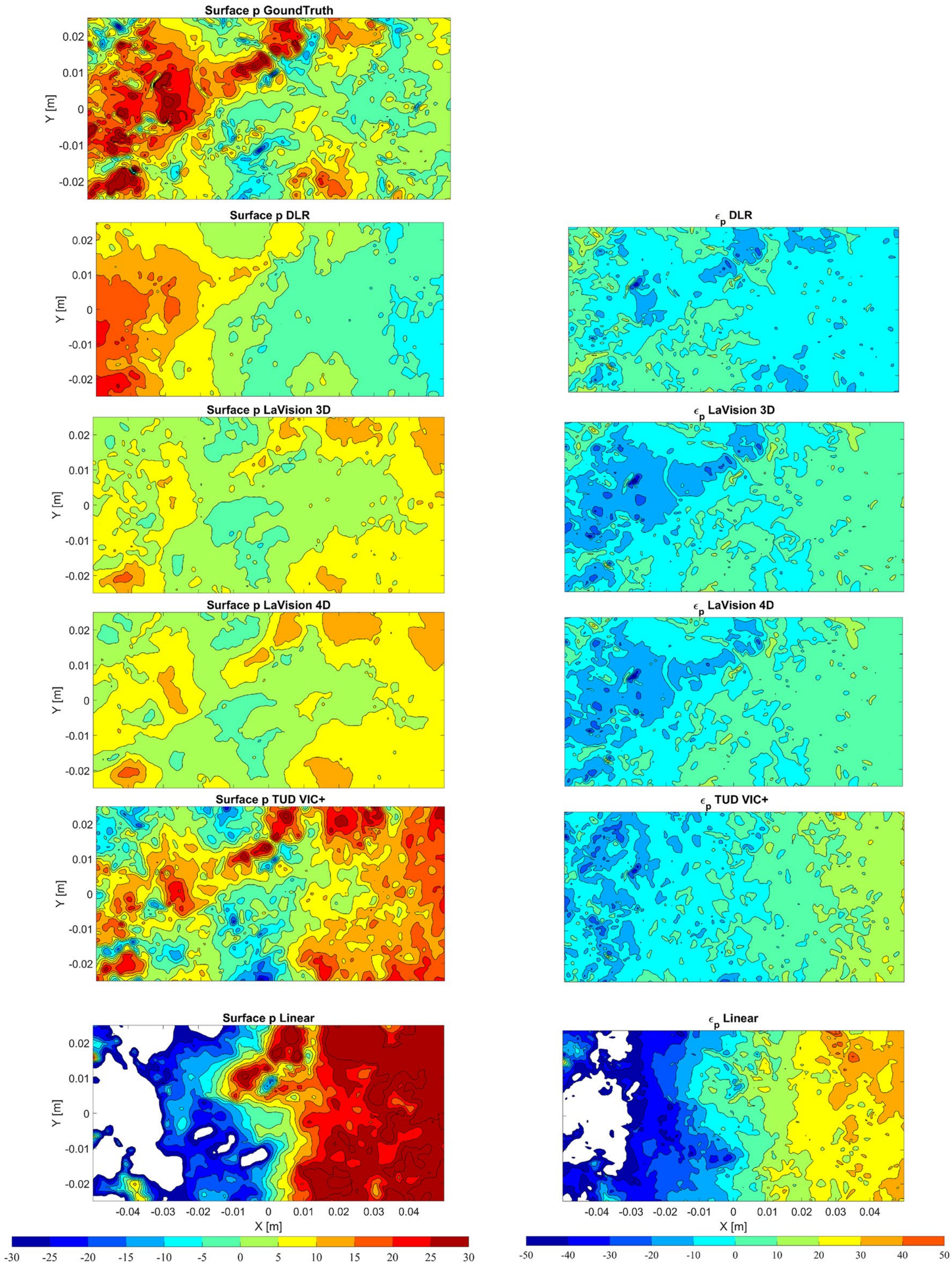

Fig. 16 Surface static pressure field (left column) and error of the static pressure (right column), evaluated at Z = 0.01 mm from the wall, for the case *ppp* = 0.025. First row: ground-truth result. The values in the colorbars are in Pascal. The colorbars at the bottom apply to all the contours of the same column

in noisier pressure fields. The pressure spectrum of the TUD VIC + algorithm agrees well with the ground-truth result at the two larger seeding concentrations, whereas at *ppp* = 0.005 it overestimates the pressure fluctuations at the lower wave numbers ($k < 20\ \mathrm{m}^{-1}$) and underestimates them at the higher wave numbers.

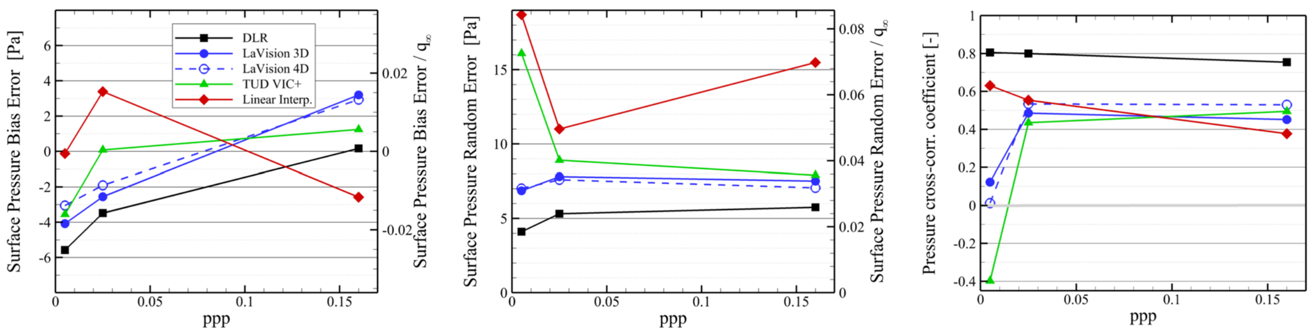

Fig. 17 Mean bias error (left), random error (middle) and cross-correlation coefficient with respect to the ground truth of the surface pressure, evaluated in the plane Z = 0.01 mm, as a function of the *ppp*. The symbol keys apply to all plots

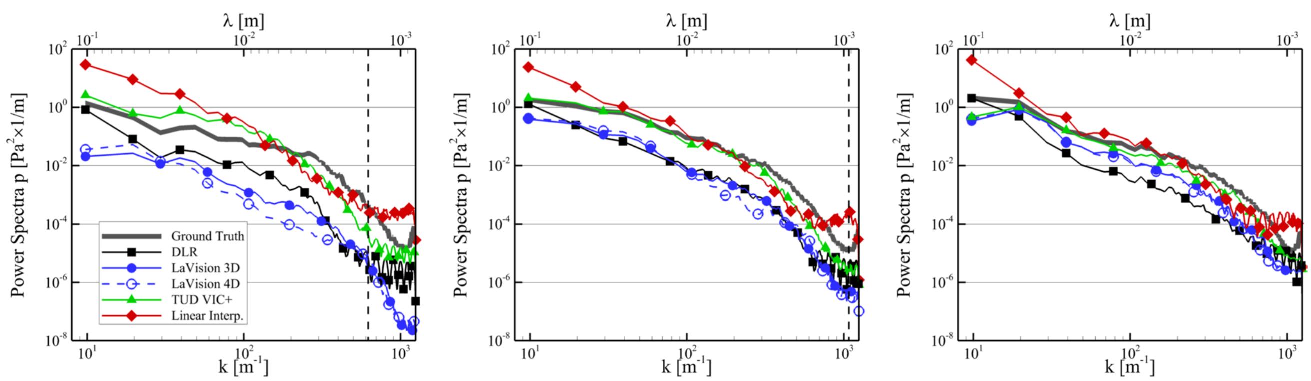

Fig. 18 Power spectral density of the surface static pressure, evaluated in the plane Z = 0.01 mm. Left: *ppp* = 0.005; middle: *ppp* = 0.025; right: *ppp* = 0.16. The bottom horizontal axis represents the wavenumber, while the top horizontal axis represents the corresponding wavelength. The dashed vertical line, when present, corresponds to the wavenumber (or wavelength) associated with the average inter-particle spacing. The symbol keys apply to all plots

4.2 Flexible panel case (metal plate)

The data assimilation results of the metal plate, with low marker concentration on the plate (*LD* case), are discussed here, for the three *ppp* values of 0.02, 0.08 and 0.16 of the flow seeding density. In Fig. 19, we illustrate the streamwise velocity component in the spanwise median plane (Y = 0 mm), for the lowest (left column) and the highest (right column) flow seeding concentrations. We recall that, for the present flexible panel case, it has been chosen to consider a virtual setup with air as the working fluid, with a free-stream velocity $U_\infty = 10m/s$, as in the numerical simulation. Also, as mentioned in Sect. 2.4, even though the lower wall has a curvilinear shape at the considered instant, for simplicity of the post-processing, the requested output has also been chosen on a parallelepipedal domain, similar to the fixed panel case. Therefore, contrary to the preceding case, a part of the near-wall region is not included in the analysis here. The presence of a vertical (wall-normal) velocity gradient is evident, where the higher velocities above the free-stream value are found in the top of the measurement domain, whereas the velocity decreases to zero at the wall. The flow is clearly turbulent, with large fluctuations attributed not only to the turbulent boundary layer, but also to the Kármán vortex street in the wake of the cylinder. The results from all the data assimilation algorithms reproduce correctly the main flow feature of the ground-truth velocity field; however, as expected and similar to the fixed panel case, the results obtained at the lowest seeding concentration (left column) exhibit larger spatial modulation effects and therefore underestimate the velocity fluctuations in the flow field.

When looking at the static pressure contour at the median plane (Fig. 20), relatively high pressure is found at the location of the panel centre (X = 0), from which the pressure decreases radially. Such high static pressure is ascribed to the downward deflection of the panel at the considered time instant, which induces a local deceleration of the flow. Additionally, a low-pressure structure is located at about –0.04 m < X < –0.03 m, which is caused by a vortex shed by the cylinder. All data assimilation algorithms correctly reproduce both the high-pressure region induced by the panel deflection and the low-pressure region in the vortex core, although, as expected, the pressure peak in the latter

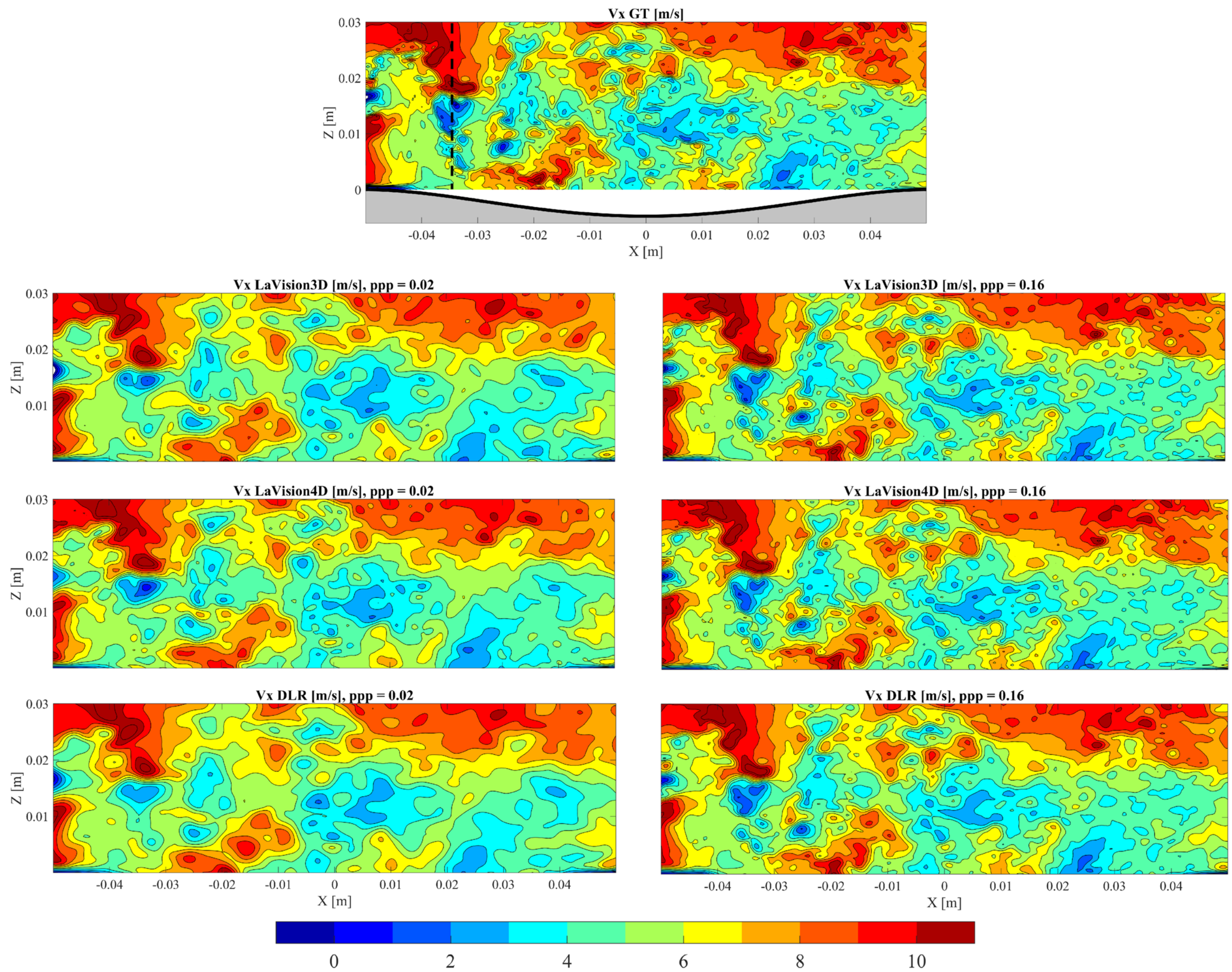

Fig. 19 Comparison of contours of the streamwise velocity component in m/s at the median plane Y = 0 mm. Top row: ground-truth flow field (velocity field only showed in the domain where the participants' outputs were requested); second row: LaVision 3D evaluation; third row: LaVision 4D evaluation; fourth row: DLR evaluation. Left: results at *ppp* = 0.02; right: results at *ppp* = 0.16. The position of the deformed panel is shown as a continuous black line in the ground-truth result. The vertical dashed line indicates the location of the profile where velocity values are extracted for the analysis in Fig. 21. The colorbar applies to all contours

is attenuated, especially at the lowest seeding concentration. To quantify the errors of the estimated velocity and static pressure, a vertical profile passing through the vortex core (X = –0.34 mm) is extracted; the velocity and static pressure along this profile are shown in Fig. 21. The velocity results, illustrated in Fig. 21-left, show a good agreement between the ground-truth velocity and those estimated by the different data assimilation algorithms, with the peak velocity values correctly reproduced; however, at the lowest seeding concentration *ppp* = 0.02, the estimated velocities exhibit unphysical oscillations in the flow zone above the vortex (Z > 20 mm), similar to Gibbs phenomenon for Fourier analysis (Helmberg 1994). The pressure results, shown in Fig. 21-right, illustrate the effect of spatial modulation in the computed pressure fields: although the two low-pressure peaks at Z = 16 mm and Z = 10 mm are correctly reproduced, their actual values are underestimated by up to 20% at *ppp* = 0.16 and 30% at *ppp* = 0.02. Small differences among the data assimilation algorithms are noticed, with the highest accuracy achieved via the use of temporal information (LaVision 4D algorithm), and higher modulation effects obtained with the DLR algorithm.

Figure 22 summarizes the mean bias and random errors of the velocity magnitude (left) and static pressure (right) for the three algorithms at the three *ppp* values. As expected, the errors decrease with increasing *ppp*, which is ascribed to the ability to resolve smaller length scales in the flow when the seeding concentration is higher. Also, especially at the higher *ppp*, the use of the temporal information in the data assimilation algorithm (LaVision 4D) enhances the accuracy

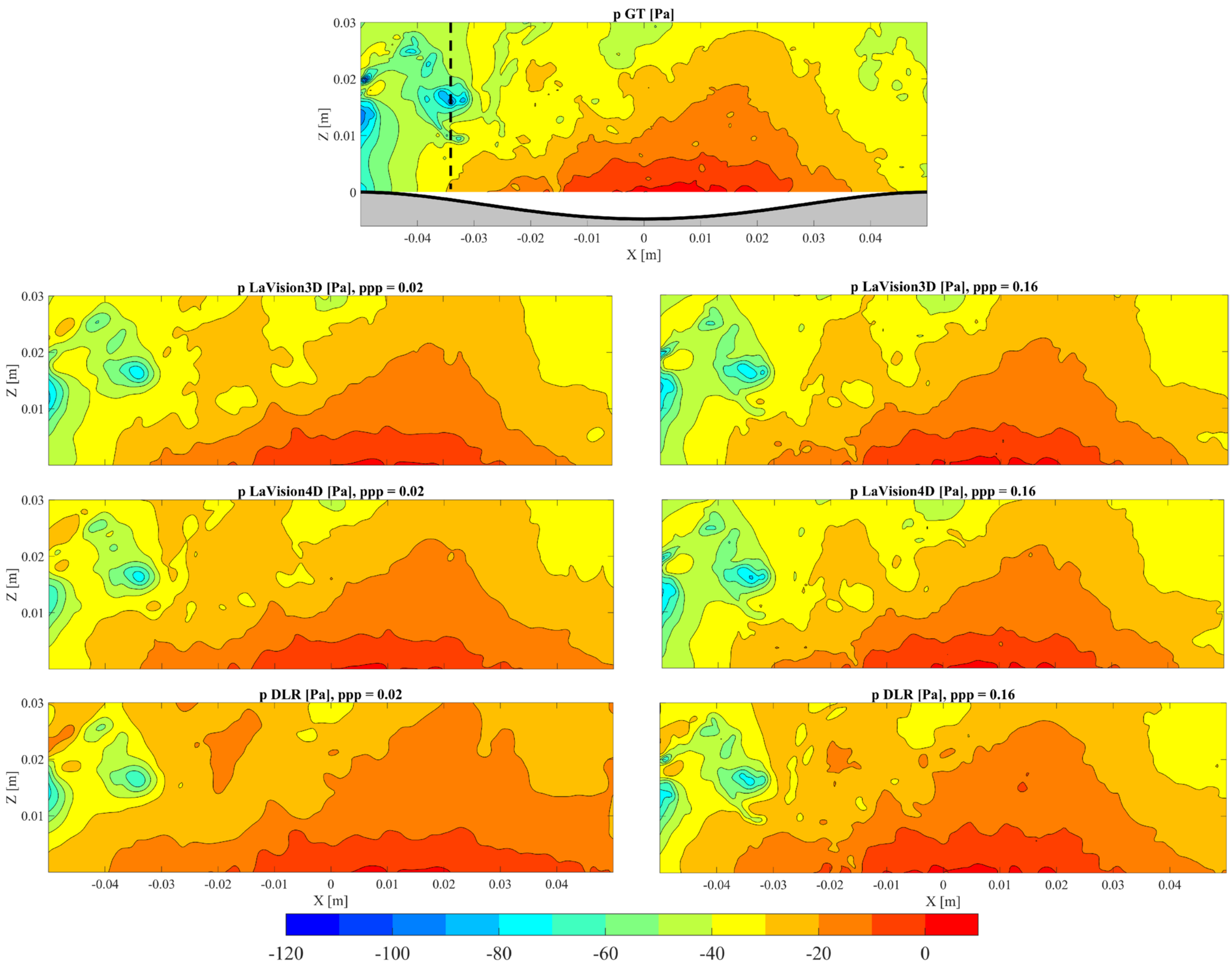

Fig. 20 Comparisons of contours of the static pressure in Pa at the median plane Y = 0 mm. Top row: ground-truth flow field (pressure field only showed in the domain where the participants' outputs were requested); second row: LaVision 3D evaluation; third row: LaVision 4D evaluation; fourth row: DLR evaluation. Left: results at *ppp* = 0.02; right: results at *ppp* = 0.16. The position of the panel is shown as a continuous black line in the ground-truth result. The vertical dashed line indicates the location of the profile where pressure values are extracted for the analysis in Fig. 21. The colorbar applies to all contours

of the results, leading to smaller errors with respect to the LaVision 3D and DLR algorithms. For the velocity, the mean bias errors are within 0.1 m/s or 1% of the free-stream velocity, whereas the random errors decrease from about 1 m/s (10% V_∞) at the lowest *ppp* to below 0.5 m/s (5% V_∞) at the highest *ppp*. For the static pressure, instead, larger differences among the data assimilation algorithms are noticed: the DLR algorithm yields the largest mean bias errors (12 to 9 Pa, or 20% to 15% of the free-stream dynamic pressure $q_\infty = 61$ Pa), whereas lower mean bias errors (4 to 8 Pa, 6.6% and 13% of q_∞) are achieved with the LaVision 3D and 4D algorithms. The bias errors are larger than the random errors, which remain between 3 and 6 Pa for the DLR algorithm, and between 2 and 5 Pa for the LaVision algorithms. It is noticed that the latter result is opposite to that discussed for the static panel case discussed in Sect. 4.1.3, whereby the random errors were larger than the systematic errors. In this case, the downward deflection of the panel causes a deceleration of the flow and therefore a pressure increase above the panel, whose magnitude is underestimated by the different DA algorithms, thus yielding large systematic errors of the static pressure.

From the analysis of the power spectra of the wall-normal velocity component V_Z, illustrated in Fig. 23, the different accuracies of the velocity reconstructions at different *ppp* values emerge. As expected, the power spectra from data assimilation algorithms agree with the ground-truth spectrum at the lowest wave numbers (larger wave lengths λ). Instead, at higher wave numbers, the reconstructed flow fields strongly modulate the velocity fluctuations, resulting

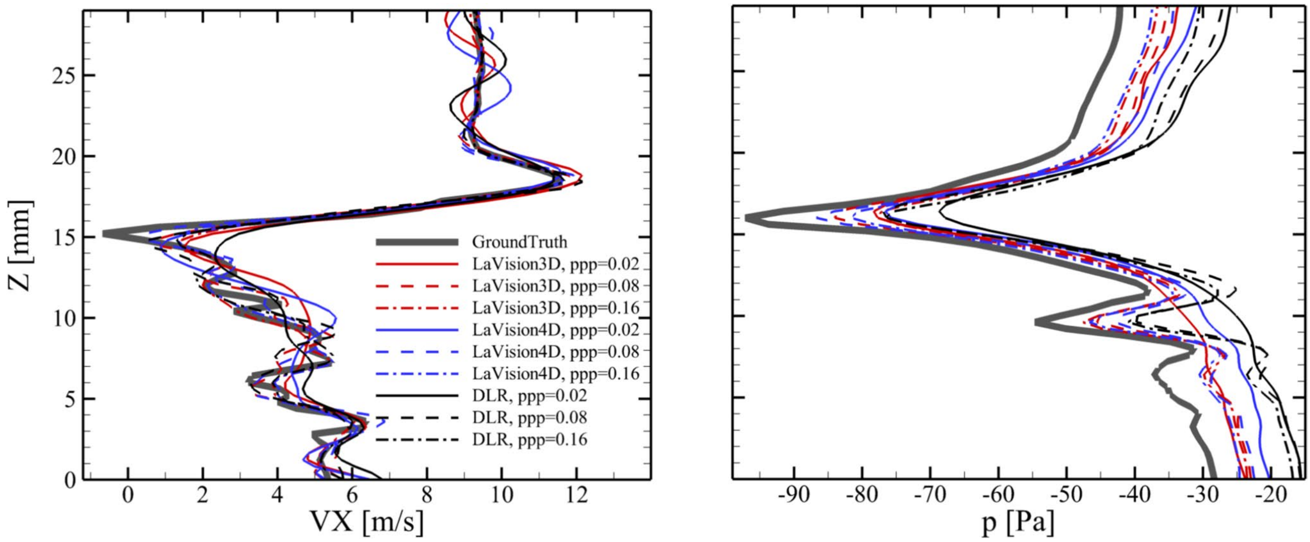

Fig. 21 Vertical profiles of instantaneous streamwise velocity (left) and static pressure (right) at $X = -34$ mm and $Y = 0$ mm. The symbol keys apply to both plots

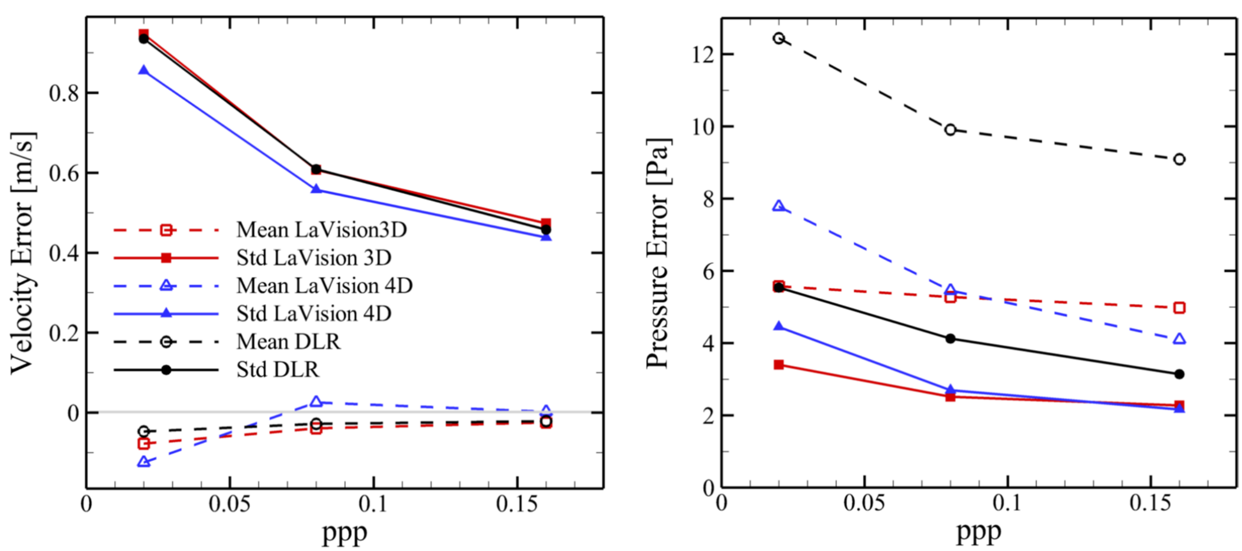

Fig. 22 Mean bias and random (std) error of the velocity magnitude (left) and of the static pressure (right) in the flow field, as a function of the ppp. The symbol keys apply to both plots

in lower values of the power spectra. In particular, at the lowest *ppp* of 0.02, the measured spectra start departing from the ground-truth one already at k ~ 160 m^{-1} (λ ~ 6 mm) (DLR algorithm) or around k ~ 200 m^{-1} (λ ~ 5 mm) (LaVision 3D or LaVision 4D). Instead, at the higher *ppp* values, the measured spectra follow the ground-truth one up to k ~ 300 m^{-1} (λ ~ 3 mm) at *ppp* = 0.08 and k ~ 360 m^{-1} (λ ~ 2.8 mm) at *ppp* = 0.16, hence enabling to resolve accurately flow length scales as small as 1/3 of the cylinder diameter or four times the inter-particle distance. For this spectral analysis, only minor differences are noticed when making use of the temporal information in the data assimilation approach (LaVision 4D vs LaVision 3D approaches).

Figure 24 shows the ground-truth panel position (left column) and surface pressure (right column) for the ground truth (top row) and the different data assimilation algorithms. The considered seeding density is *ppp* = 0.02. It is remarked here that the indicated seeding density corresponds to the concentration of tracer particles in the flow (not on the panel surface); hence, its variation is expected to have negligible effect on the accuracy of the reconstruction of the panel position. At the considered time instant,

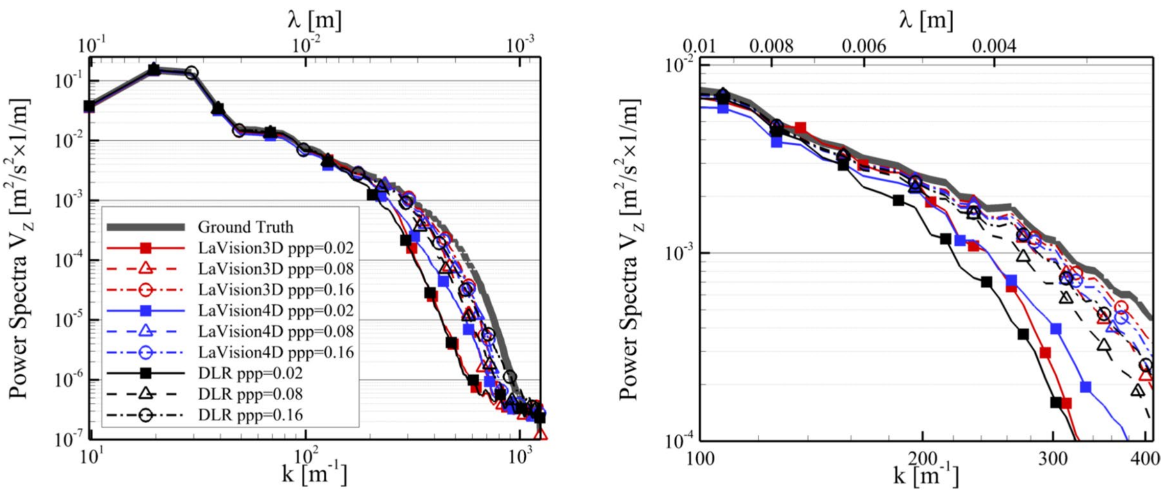

Fig. 23 Power spectra of the wall-normal velocity component V_Z. Left: entire spectra; right: detail for wave numbers between 100 and 410 m^{-1}. The symbol keys apply to both plots. It is reminded that the average inter-particle distances for cases $ppp = 0.02$, 0.08 and 0.16 are $\lambda = 1.3$ mm, 0.82 mm and 0.65 mm, respectively, corresponding to wave numbers $k = 769$ m^{-1}, 1220 m^{-1} and 1538 m^{-1}, respectively

the panel is deflected downwards reaching $Z = -4.75$ mm at its centre. The panel position is reconstructed with very high accuracy by all data assimilation algorithms, with only minor differences with respect to the true position, mainly at the panel edges; this indicates that the number of markers on the panel is large enough compared to the shape complexity of the panel, that is indeed characterized by only large-scale variations. The surface pressure is the minimum towards the upstream edge the panel ($X < -40$ mm) and reaches its maximum value $p_{max} = 23$ Pa at the panel centre due to the flow deceleration caused by the panel deflection. The reconstructed surface pressure field (Fig. 24 right) reproduces correctly the trend of the ground-truth surface pressure, and in particular the low pressure at the upstream edge of the domain and the high pressure at the centre of the panel; however, the magnitudes of both the minimum and the maximum pressure values are clearly underestimated.

To quantify the accuracy of the data assimilation algorithm, profiles of the panel position and surface static pressure are extracted along $X = 0$ mm and presented in Fig. 24. The deflection of the panel, shown in Fig. 24-left, is correctly captured by all algorithms with an accuracy within 10 μm, which is only slightly higher than the noise added to the marker positions, equal to $0.1\ \overline{px} = 8.67\mu m$. It should be noticed that, in Fig. 24-left, the results of the LaVision 3D algorithm are not visible because, due to the slow motion of the panel, they coincide with those of the LaVision 4D algorithm. Larger discrepancies are instead encountered in the static pressure result illustrated in Fig. 24-right: the ground-truth pressure field exhibits a pressure peak of 24 Pa at $Y = 0$. Although the presence of the pressure peak is retrieved by all the data assimilation algorithms, its value is underestimated by 45% to 65% depending on the seeding concentration and the algorithm employed. As expected, the largest modulation occurs at the lowest seeding density of $ppp = 0.02$. Among the different algorithms, the highest accuracy is achieved via the LaVision 3D and 4D evaluations (Fig. 25).

A quantitative analysis of the mean bias and random errors of the panel position and surface pressure are reported in Fig. 26, considering the DLR, LaVision 3D and LaVision 4D algorithms and the three *ppp* values. The position errors (Fig. 26-left) are independent of the *ppp* and the data assimilation algorithm, and attain values of –5 μm and 5 μm for the mean bias and random components, respectively, which correspond to 0.1% of the panel maximum deflection or less than 60% of the random noise of the markers (equal to $0.1\ \overline{px} = 8.67\mu m$). Such a behaviour is quite logical as the marker density is the same throughout, but also indicates that the accuracy of marker detection was not affected by the increase in particle density. Also for the surface pressure (Fig. 26-right), the results obtained with the three algorithms show similar trends. The increase of *ppp* yields a decrease of the random errors in the range 8 Pa to 3 Pa (16% to 5% of q_∞). The DLR algorithm exhibits mean bias errors between 12 and 9 Pa decreasing with the seeding concentration, whereas for the LaVision algorithms the mean bias error slightly increases in magnitude, especially for the LaVision 4D algorithm, reaching –4 Pa at the highest *ppp*.

5 Conclusions

This work presents an assessment of the accuracy of data assimilation algorithms for the dense reconstruction of flow fields, conducted within the framework of the European Union Horizon 2020 project HOMER (Holistic Optical

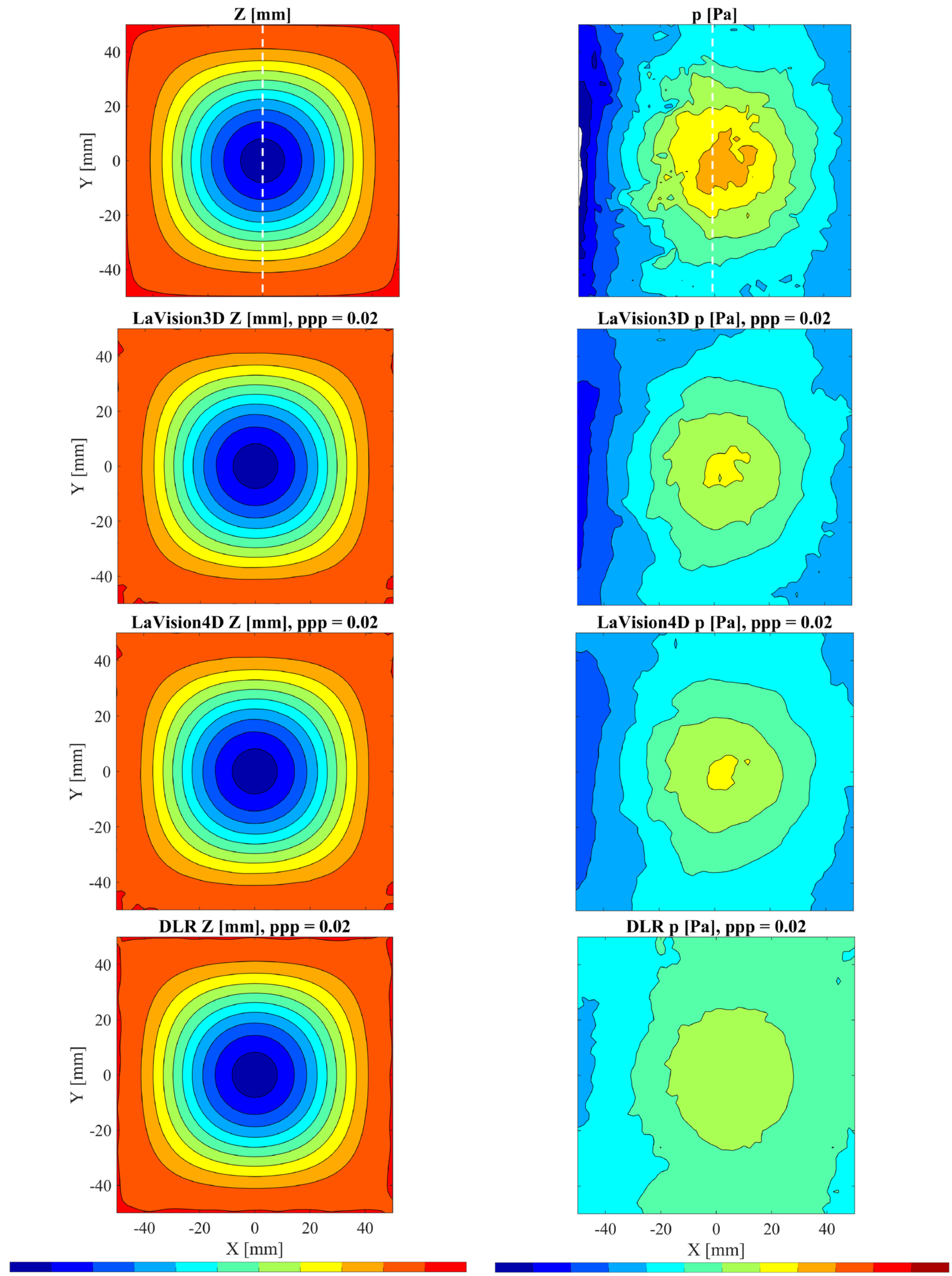

Fig. 24 Panel Z-position in mm (left) and surface pressure in Pa (right). First row: ground-truth result; second row: LaVision 3D evaluation; third row: LaVision 4D evaluation; fourth column: DLR evaluation. All evaluations are conducted at $ppp = 0.02$. The dashed vertical line represents the location of the profile extracted for the analysis presented in Fig. 25. The colorbars at the bottom apply to all the contours of the same column

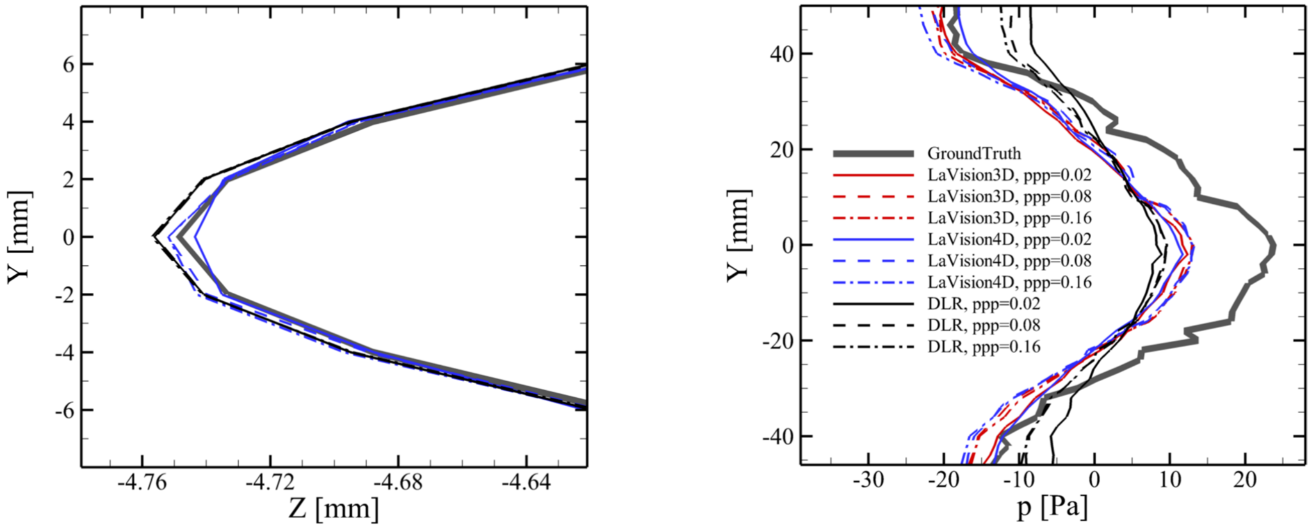

Fig. 25 Left: Detail of the panel Z-deflection along a vertical profile (only -8 mm $\leq Y \leq$ 8 mm shown for sake of clarity) at $X = 0$ mm. Right: surface pressure on the panel along a vertical profile at $X = 0$ mm

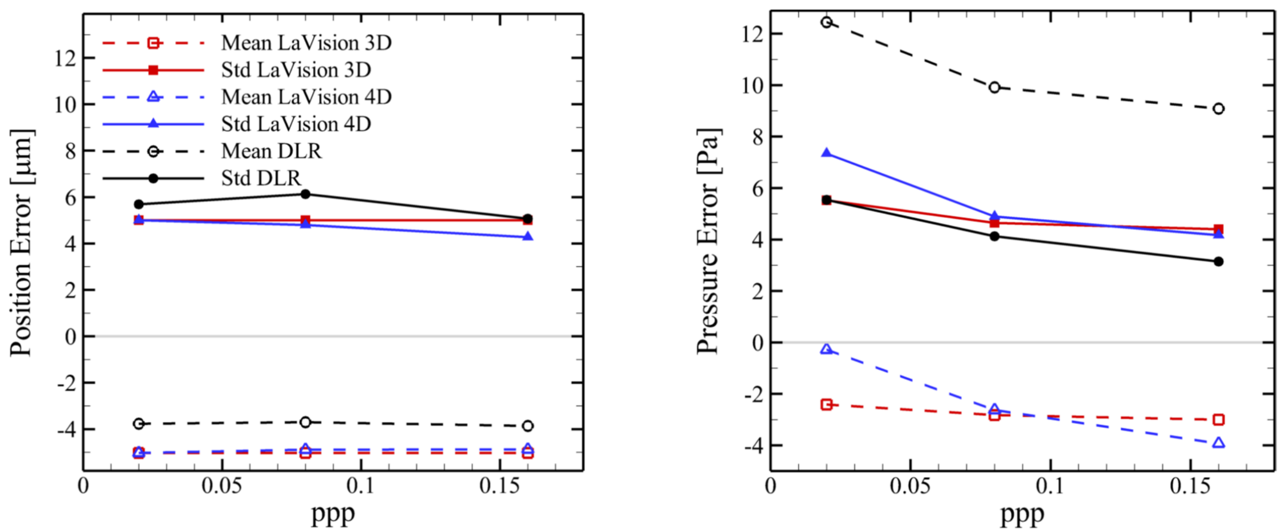

Fig. 26 Mean bias and random (std) error of the reconstructed Z-position of the panel (left) and of the surface static pressure on the panel (right), as a function of the *ppp*. The symbol keys apply to both plots

Metrology for Aero-Elastic Research). The assessment made use of a synthetic experiment reproducing the wall-bounded flow in the wake of a cylinder, considering both the cases of rigid wall and flexible panel, with the latter oscillating at a frequency comparable to frequency of the vortex shedding from the cylinder. The particle positions along their trajectories were provided to the research groups participating in the flow field reconstructions. For the rigid wall case, three datasets were considered, representative of experiments from very low ($ppp = 0.005$) to very high ($ppp = 0.16$) seeding concentration. For the flexible panel case, the seeding density was varied in the range of *ppp* values between 0.02 and 0.16; the case analysed consisted of a metal plate with low density of surface markers. The requested output quantities were the three velocity components, the nine components of the velocity gradient tensor and the static pressure, all defined in a Cartesian grid of $h = 0.4$ mm grid spacing.

Three research groups took part to the analysis of the data of the rigid wall case, namely DLR, LaVision GmbH and TU Delft. The latter two groups submitted results with two algorithms each, which make use of instantaneous information only (LaVision 3D and TUD VIC + algorithms) or also of information from previous and successive time instants (LaVision 4D and TUD TSA algorithms). The velocity fields estimated by the different data assimilation algorithms showed good agreement with the ground-truth velocity field, with errors between 3 and 11% of the bulk velocity V_∞, depending on the seeding concentration and the data assimilation algorithm. Overall, the difference in velocity errors among the different DA algorithms was mostly with 2% of V_∞, indicating that no algorithm exhibited clearly superior accuracy to the others. As the flow kinetic energy is mainly contained in the larger flow structures, these errors are of similar magnitude as those achieved when using the conventional linear interpolation of the particle velocities onto the output Cartesian grid. Hence, in the present quite ideal case where position noise is low and no outliers are present, it can be concluded that, because of its simplicity and negligible computational cost compared to the DA method, and depending on the particle density in the input data, linear interpolation can be considered a valid alternative when lower accuracy of the reconstructed flow fields is considered acceptable. However, the spectral analysis revealed that the use of the data assimilation algorithms enables to increase the range of resolved length scales by factors 3 to 4 with respect to the linear interpolation approach. The analysis of the velocity gradients highlighted the presence of bias and random errors of 100–150 Hz or 10–15% of the typical vorticity magnitude peaks. As expected, both error components decrease with increasing seeding concentration; however, even at the highest *ppp* of 0.16, bias and random errors exceeding 20 Hz and 80 Hz, respectively, are obtained. As expected, the linear interpolation of the particle velocities yielded the largest modulation of the velocity gradients, with peak vorticity values underestimated by over 25% with respect to the better-performing DA algorithm (in the specific case, LaVision 4D). Finally, the evaluated pressure featured bias errors within ± 5 Pa and random errors between 5 and 15 Pa. A better agreement with the actual pressure field was achieved away from the wall, whereas on the solid surface the agreement decreased due to the lower magnitude of the pressure fluctuations. In this case, the FlowFit2 algorithm from DLR exhibited the best performances, yielding a cross-correlation coefficient with the ground-truth pressure result exceeding 0.9 away from the wall, and of about 0.8 on the rigid wall. For the other DA algorithms, the accuracy of the surface pressure reconstruction was significantly lower, with cross-correlation coefficient values between 0 and 0.6.

The data of the datasets with a flexible panel on the ground were analysed by the LaVision and DLR research groups. Also in this case, LaVision proposed two data assimilation algorithms, without (LaVision 3D) and with (LaVision 4D) the use of information from previous and successive time instants. The analysis of the results showed that the evaluated velocity suffered from errors of up 10% of V_∞, whereas the pressure errors were up to 20% of q_∞. These errors decrease with increasing seeding concentration, with minimum errors of 5% of V_∞ for the velocity and 7% of q_∞ for the static pressure. The use of the temporal information in the data assimilation algorithm (LaVision 4D vs LaVision 3D) yielded a slight increase in the measurement accuracy especially for the velocity, quantified in a reduction of the measurement error between 5 and 10% of V_∞. When looking at the spatial power spectra of the velocity fluctuations, it was noticed that the higher *ppp* enabled to resolve accurately smaller turbulent structures in the flow. Flow scales of at least four times the inter-particle distance were correctly reconstructed with the DA algorithms. The panel position could be reconstructed within 10 μm accuracy (0.2% of the peak displacement) with all algorithms at the three *ppp* values, close to the value of the random noise added to the marker positions. The reconstructed surface pressure followed closely the trend of the ground-truth value, but exhibited both bias and random errors of the order of 10% q_∞, with clear modulation of the pressure peak value at the centre of the panel.

The data presented here as well as the additional datasets for the flexible panel test case (e.g. rubber panel, other values of markers densities, separate imaging systems for flow tracers and particle markers) will be made available online for download at https://www.onera.fr/flow-benchmarks; in this dedicated online portal, the users can upload their flow results to obtain an automatic assessment of their data assimilation algorithms in terms of errors of the estimated velocity, pressure and panel position; the online portal also provides test cases with automatic evaluation for particle tracking algorithms (Leclaire et al. 2022).

Acknowledgements The data processing performed by the research groups who participated in the challenge is kindly acknowledged.

Author contribution All authors participated in equal parts to the conceptualization of the work and the definition of the test cases. Benjamin Leclaire performed the numerical simulations and produced the test cases. Andreas Schroeder was project manager for the entire project. Andrea Sciacchitano performed the data analysis and produced the first draft of the paper. All authors critically reviewed the manuscript.

Funding This work has been carried out in the context of the HOMER (Holistic Optical Metrology for Aero-Elastic Research) project, funded by the European Union's Horizon 2020 research and innovation programme under grant agreement No 769237.

Data availability The data published in this paper is made available open access in the 4TU Research Data repository (https://data.4tu.nl/).

Declarations

Conflict of interest The authors declare no competing interests.

Open Access This article is licensed under a Creative Commons Attribution 4.0 International License, which permits use, sharing, adaptation, distribution and reproduction in any medium or format, as long as you give appropriate credit to the original author(s) and the source, provide a link to the Creative Commons licence, and indicate if changes were made. The images or other third party material in this article are included in the article's Creative Commons licence, unless indicated otherwise in a credit line to the material. If material is not included in the article's Creative Commons licence and your intended use is not permitted by statutory regulation or exceeds the permitted use, you will need to obtain permission directly from the copyright holder. To view a copy of this licence, visit http://creativecommons.org/licenses/by/4.0/.

References

Agüí J, Jimenez J (1987) On the performance of particle tracking velocimetry. J Fluid Mech 185:447–468

Azijli I, Dwight RP (2015) Solenoidal filtering of volumetric velocity measurements using Gaussian process regression. Exp Fluids 56(11):1–18

Cai S, Mao Z, Wang Z, Yin M, Karniadakis GE (2021) Physics-informed neural networks (PINNs) for fluid mechanics: a review. Acta Mech Sin 37(12):1727–1738

Cakir BO, Saiz GG, Sciacchitano A, van Oudheusden B (2022) Dense interpolations of LPT data in the presence of generic solid objects. Meas Sci Technol 33(12):124009

Chandramouli P, Mémin E, Heitz D (2020) 4D large scale variational data assimilation of a turbulent flow with a dynamics error model. J Comput Phys 412:109446

Choi JH, Lee SJ (2000) Ground effect of flow around an elliptic cylinder in a turbulent boundary layer. J Fluids Struct 14(5):697–709

Christiansen IP (1973) Numerical simulation of hydrodynamics by the method of point vortices. J Comput Phys 13(3):363–379

Dandois J, Mary I, Brion V (2018) Large-eddy simulation of laminar transonic buffet. J Fluid Mech 850:156–178

Du Y, Wang M, Zaki TA (2023) State estimation in minimal turbulent channel flow: a comparative study of 4DVar and PINN. Int J Heat Fluid Flow 1(99):109073

Ehlers F, Schröder A, Gesemann S (2020) Enforcing temporal consistency in physically constrained flow field reconstruction with FlowFit by use of virtual tracer particles. Measurement Sci Technol 31(9):094013

Elsinga GE, Scarano F, Wieneke B, van Oudheusden BW (2006) Tomographic particle image velocimetry. Exp Fluids 41(6):933–947

Gesemann S, Huhn F, Schanz D and Schröder A (2016) From noisy particle tracks to velocity, acceleration and pressure fields using B-splines and penalties. *In 18th international symposium on applications of laser and imaging techniques to fluid mechanics, Lisbon, Portugal (pp. 4–7)*

Helmberg G (1994) The gibbs phenomenon for Fourier interpolation. J Approx Theory 78(1):41–63

Jeon YJ, Schneiders JFG, Müller M, Michaelis D and Wieneke B (2018) 4D flow field reconstruction from particle tracks by VIC+ with additional constraints and multigrid approximation. *In Proceedings 18th International Symposium on Flow Visualization, ETH Zurich*

Jeon YJ (2021) Eulerian time-marching in Vortex-In-Cell (VIC) method: reconstruction of multiple time-steps from a single vorticity volume and time-resolved boundary condition. *In 14th International Symposium on Particle Image Velocimetry – ISPIV 2021, August 1–5, 2021*

Jeon YJ, Müller M, Michaelis D (2022) Fine scale reconstruction (VIC#) by implementing additional constraints and coarse-grid approximation into VIC+. Exp Fluids 63:70

Last G, Penrose M. Lectures on the Poisson process. Cambridge University Press; 2017 Oct 26. https://www.math.kit.edu/stoch/~last/seite/lectures_on_the_poisson_process/media/lastpenrose2017.pdf

Leclaire B, Cornic P, Champagnat F, Fabre E and Calmels F (2022) A web portal for automatic performance evaluation of Lagrangian Particle Tracking and Data Assimilation algorithms. *In 20th International Symposium on the Application of Laser and Imaging Techniques to Fluid Mechanics, Lisbon, Portugal*.

Liu DC, Nocedal J (1989) On the limited memory BFGS method for large scale optimization. Math Program 45(1):503–28

Malik NA, Dracos T, Papantoniou DA (1993) Particle tracking velocimetry in three-dimensional flows. Exp Fluids 15(4):279–294

Mons V, Marquet O, Leclaire B, Cornic P, Champagnat F (2022) Dense velocity, pressure and Eulerian acceleration fields from single-instant scattered velocities through Navier–Stokes-based data assimilation. Meas Sci Technol 33(12):124004

Scarano F (2012) Tomographic PIV: principles and practice. Meas Sci Technol 24(1):012001

Scarano F, Schneiders JFG, Gonzalez Saiz G, Sciacchitano A (2022) Dense velocity reconstruction with VIC-based time-segment assimilation. Exp Fluids 63(6):96

Schanz D, Gesemann S, Schröder A (2016) Shake-the-box: lagrangian particle tracking at high particle image densities. Exp Fluids 57(5):1–27

Schiavazzi D, Coletti F, Iaccarino G, Eaton JK (2014) A matching pursuit approach to solenoidal filtering of three-dimensional velocity measurements. J Comput Phys 263:206–221

Schlatter P, Li Q, Brethouwer G, Johansson AV, Henningson DS (2010) Simulations of spatially evolving turbulent boundary layers up to Re_θ= 4300. Int J Heat Fluid Flow 31(3):251–261

Schneiders JFG, Scarano F (2016) Dense velocity reconstruction from tomographic PTV with material derivatives. Exp Fluids 57(9):1–22

Schröder A, Schanz D (2023) 3D Lagrangian particle tracking in fluid mechanics. Annu Rev Fluid Mech 55:511

Sciacchitano A, Leclaire B and Schröder A (2021) Main results of the first Data Assimilation Challenge. *In 14th International Symposium on Particle Image Velocimetry – ISPIV 2021, 1–5, 2021*

Sperotto P, Ratz M, Mendez MA (2024) SPICY: a python toolbox for meshless assimilation from image velocimetry using radial basis functions. J Open Sourc Softw 9(93):5749

van Oudheusden BW (2013) PIV-based pressure measurement. Meas Sci Technol 24(3):032001

Welch P (1967) The use of fast Fourier transform for the estimation of power spectra: a method based on time averaging over short, modified periodograms. IEEE Trans Audio Electroacoust 15(2):70–73

Publisher's Note Springer Nature remains neutral with regard to jurisdictional claims in published maps and institutional affiliations.